

# Subharmonic eigenvalue orbits in the spectrum of pulsating Poiseuille flow

J.S. Kern<sup>1,†</sup>, A. Hanifi<sup>1</sup> and D.S. Henningson<sup>1</sup>

<sup>1</sup>FLOW Turbulence Laboratory, Department of Engineering Mechanics, KTH Royal Institute of Technology, SE-100 44 Stockholm, Sweden

(Received 8 October 2021; revised 14 April 2022; accepted 6 June 2022)

Spectral degeneracies where eigenvalues and eigenvectors simultaneously coalesce, also known as exceptional points, are a natural consequence of the strong non-normality of the Orr–Sommerfeld operator describing the evolution of infinitesimal disturbances in parallel shear flows. While the resonances associated with these points give rise to algebraic growth, the development of non-modal stability theory exploiting specific perturbation structures with much larger potential for transient energy growth has led to waning interest in spectral degeneracies. The appearance of subharmonic eigenvalue orbits, recently discovered in the periodic spectrum of pulsating Poiseuille flow, can be traced back to the coalescence of eigenvalues at exceptional points. We present a thorough analysis of the spectral properties of the linear operator to identify exceptional points and accurately map the prevalence of subharmonic eigenvalue orbits for a large range of pulsation amplitudes and frequencies. This information is then combined with solutions of the linear initial value problem to analyse the impact of the appearance of these orbits on the temporal evolution of linear disturbances in pulsating Poiseuille flow. The periodic amplification phases are shown to be heralded by repeated non-normal growth bursts that are intensified by the formation of subharmonic orbits involving the leading eigenvalues. These bursts are associated with the change of alignment of the perturbation from the decaying towards the amplified branch of the subharmonic eigenvalue orbits in a so-called branch transition process.

**Key words:** shear-flow instability, channel flow

## 1. Introduction

Linear stability analysis is a standard tool to assess the stability characteristics of a flow case by linearising the full nonlinear system of equations and analyse

† Email address for correspondence: [skern@kth.se](mailto:skern@kth.se)

the growth or decay of infinitesimal disturbances. In the case of parallel viscous shear flows with a single inhomogeneous spatial direction the normal mode ansatz leads to the Orr–Sommerfeld–Squire (OS–SQ) equations that govern the evolution of three-dimensional, wave-like perturbations (Orr 1907; Sommerfeld 1908; Squire 1933). The distinction between stable and unstable flows in the time-asymptotic limit is made by determining whether the eigenvalues of the linearised operator are all contained in the stable half-plane. Due to the considerable non-normality of the OS operator, a full description of perturbation growth needs to take into account the details of the initial condition that can lead to important transient, non-modal energy growth due to the superposition of non-orthogonal eigendirections even if the system is linearly stable (Reddy & Henningson 1993; Trefethen *et al.* 1993; Schmid 2007).

A less well known consequence of the non-normality of the OS operator is the possibility of spectral degeneracy, i.e. simultaneous coalescence of two or more eigenstates. Such a degeneracy has been reported in early works by Betchov & Criminale (1966) in the analysis of inviscid jets and wakes. Soon thereafter, Gaster (1968) showed why such degeneracies must occur by considering the analyticity of the eigenvalue expansions for the viscous problem involving the OS operator. Following these discoveries, a series of studies by Gaster & Jordinson (1975), Jones (1988) and Or (1991) fleshed out the mathematical structure of the eigenvalue degeneracies and identified some of their notorious consequences such as the high sensitivity of the eigenvalues close to the points of coalescence. In seminal work by Gustavsson & Hultgren (1980), an algebraic growth mechanism based on coalescence of the eigenvalues of the OS operator and the homogeneous SQ operator was identified. This resonance mechanism was subsequently studied for the temporal and spatial branches of Blasius boundary layer flows (Koch 1986) and plane Poiseuille flow (Gustavsson 1986; Shanthini 1989). Although algebraic growth stemming from spectral degeneracies and near-degeneracies was identified, the specific shape of the initial disturbance was not considered, which can generate considerably more growth via non-modal mechanisms that do not depend on spectral degeneracies (Farrell 1988; Butler & Farrell 1992; Reddy & Henningson 1993; Reddy, Schmid & Henningson 1993). These studies of transient growth also concluded that eigenvalue degeneracies are neither necessary nor sufficient to explain transient energy growth in steady flows (Reddy & Henningson 1993; Reddy *et al.* 1993).

With the advent of this more general framework for non-modal stability, the interest in spectral degeneracies of the OS operator has decreased. Meanwhile, the specific case of eigenvalue coalescence in the OS operator has been put into wider context and connected to the concept of exceptional points (EPs) (Kato 1976). Exceptional points describe the simultaneous coalescence of eigenstates (eigenvalues and eigenvectors) that naturally occur for non-normal parameter dependent operators and are intrinsically linked to the non-orthogonality of the eigenvector basis. In fact, fluid mechanics is only one of many fields of physics in which EPs have been identified and play an important role. Especially in optics as well as quantum and nuclear physics, the effects of EPs have been studied extensively both theoretically and experimentally (see Heiss (2012) for a recent review of the topic). One feature of EPs that is of particular interest in the context of this study is that when eigenvalues are traced along a path in the complex plane that encloses an EP, these eigenvalues may change place (see e.g. Zhong (2019) and Luitz & Piazza (2019) for applications in optics and theoretical physics or Mensah *et al.* (2018) and Ghani & Polifke (2021) for recent works in theoretical and experimental thermoacoustics). This phenomenon is often called ‘eigenvalue braiding’ or ‘eigenvalue switching’, which is not to be confused with a different concept of the same name, more spread in the fluid

dynamics community, that refers to the switching of the dominant mode between two distinct eigenpairs as a control parameter is varied (see e.g. Chang, Chen & Straughan 2006). In recent years, the experimental and theoretical study of eigenvalue switching and other topological phenomena related to the encircling of EPs have gathered much interest in physics, in particular quantum physics, microwave physics, optics and acoustics (Dembowski *et al.* 2001; Lee *et al.* 2009; Doppler *et al.* 2016; Özdemir *et al.* 2019; Ghani & Polifke 2021). To the authors' knowledge, no such work has been carried out within fluid mechanics.

While several studies considered and identified eigenvalue degeneracies for steady flow configurations, in particular plane Poiseuille flow (Gustavsson 1986; Jones 1988; Shanthini 1989), little is known about the prevalence of EPs and their impact on the evolution in time of the instantaneous spectrum in unsteady flow cases such as pulsating Poiseuille flow. To the authors' knowledge, eigenvalue degeneracies for this flow case are mentioned only in the pioneering work by Grosch & Salwen (1968), where they are noted in passing, as well as in a recent study applying the optimally time-dependent (OTD) modes to pulsating Poiseuille flow (Kern *et al.* 2021). In the latter, the coalescence of nearby eigenvalue orbits is conjectured to be the reason for the appearance of subharmonic orbits in the eigenvalue traces of the reduced operator. When considering the effect of EPs and, more generally, the instantaneous spectra on the evolution of a linear perturbation, a relevant measure is the time scale separation between the intrinsic time scales of the perturbations and the time-dependence of the base flow (Davis 1976). When the temporal variation of the base flow is sufficiently slow compared with the instabilities that develop on top of it, the local spectra (in time) are expected to dominate the evolution of the linear perturbation. The implications of this prediction are particularly interesting in view of the formation of subharmonic eigenvalue orbits via eigenvalue braiding at EPs.

The aim of this paper is two-fold. The first goal is a detailed analysis of the instantaneous temporal spectrum of the OS operator applied to pulsating Poiseuille flow. This includes the identification of eigenvalue degeneracies as EPs that are responsible for the formation of subharmonic eigenvalue orbits, the exploration of the range of pulsation frequencies and amplitudes that support such orbits as well as a study of the impact of base flow pulsations on the maximum non-normal growth potential. In a second part, we consider the impact of the instantaneous spectral properties of the operator on the evolution of a linear perturbation over a range of pulsation frequencies and amplitudes and how these are influenced by the appearance of subharmonic eigenvalue orbits.

The remainder of this paper is structured as follows. In § 2 we introduce the concept of EPs within the context of eigenvalue decompositions of parameter dependent matrices that lead to the occurrence of subharmonic eigenvalue orbits in periodic cases. We then review the geometry and the governing equations of pulsating Poiseuille flow (§ 3). Details of the numerical methods can be found in Appendix A. The main body of the paper is divided into two parts. The first is dedicated to the subharmonic eigenvalue orbits in the local problem, in which we identify them in the spectrum of pulsating Poiseuille flow (§ 4.1), analyse their prevalence as a function of pulsation frequency and amplitude (§ 4.2) and discuss limiting cases based on a time scale analysis (§ 4.3). In a final section we consider the variation of the maximum non-normal growth potential during a pulsation period (§ 4.4). The second part of the paper, § 5, investigates the impact of the subharmonic eigenvalue orbits on solutions of the linear initial value problem (IVP). We conduct a detailed analysis of the effect of EPs and subharmonic eigenvalue orbits on the evolution of two-dimensional linear perturbations in pulsating Poiseuille flow for varying pulsation frequencies and amplitudes (§§ 5.1 and 5.2) and relate the results to Floquet theory (§ 5.3).

After a brief outlook on the effect of variations of the Reynolds number and the streamwise wavenumber (§ 5.4) and three-dimensional perturbations (§ 5.5), a summary of the results and concluding remarks are gathered in § 6. An interesting link between the subharmonic eigenvalue orbits in the spectrum of pulsating Poiseuille flow and those documented using OTD modes is elucidated in Appendix C.

## 2. Mathematical background

We follow Kato (1976) in this section describing the mathematical background of eigenvalue orbits of matrices with parameter dependent elements.

### 2.1. Parameter dependent matrices

Consider the matrix  $A \in \mathbb{C}^{n \times n}$ , whose elements  $a_{ij}$  are analytic functions of the parameters  $p = (p_1, \dots, p_m) \in \mathbb{R}^m$  and  $t \in \mathbb{R}$  such that

$$A(p, t) = A(p, t + T), \quad \forall t \in \mathbb{R}, \tag{2.1}$$

where  $T$  is the period of the parameter  $t$ . To simplify notation we will in the following sometimes omit the explicit dependence on  $p$  and  $t$  where it is evident. We are interested in the parameter dependent eigenstates  $(\lambda, \xi)$  of  $A$  given by the relation

$$A\xi_i = \lambda_i\xi_i, \quad i = 1, \dots, s, \tag{2.2}$$

where  $\lambda_i \in \mathbb{C}$  is the eigenvalue,  $\xi_i \in \mathbb{C}^n$  is the corresponding (right) eigenvector and  $1 \leq s \leq n$  is the number of distinct eigenvalues.

We denote by  $\Lambda(A) = \{\lambda_i\}_{1, \dots, s}$  the spectrum of  $A$ . Due to the periodicity of  $a_{ij}$  with respect to  $t$  we have

$$\Lambda(A(p, t)) = \Lambda(A(p, t + T)), \quad \forall t \in \mathbb{R}. \tag{2.3}$$

Note that the spectrum depends on all the parameters pointwise and is therefore independent of the smoothness of  $a_{ij}$  with respect to  $p$  and  $t$ . In fact, for (2.3) to hold,  $a_{ij}$  need not even be a continuous function of the parameters.

### 2.2. Eigenvalue trajectories and EPs

We now consider the change of the eigenstates as the parameters  $p$  and  $t$  are varied and in particular the question of whether the eigenvalue trajectories  $\lambda_i(p, t)$  form smooth periodic orbits in the complex plane as  $t$  traverses a period for a fixed  $p$ . In mathematical terms, we want to determine whether the analyticity of the coefficients of  $A$  with respect to the parameters carries over to the eigenvalue trajectories. Note that this analyticity combined with the pointwise dependence of the spectrum on the parameters lets us already conclude that the eigenvalue trajectories are continuous, i.e. that they will form periodic orbits.

If the matrix  $A$  is normal for all  $p, t \in \mathbb{R}$ , then  $A$  is always diagonalisable, the eigenbasis  $\mathcal{E} = [\xi_1, \dots, \xi_s]$  is orthogonal and of full rank ( $s = n$ ) and all eigenstates are analytic functions of  $p$  and  $t$  (Kato 1976). It immediately follows that the eigenvalue trajectories are smooth closed curves in the complex plane that inherit the periodicity with respect to  $t$ .

In the case of a non-normal matrix  $A$ , the situation is more complicated since the eigenvectors are non-orthogonal. In this context it is possible for two eigenstates to simultaneously coalesce leading to a degeneracy of the corresponding eigenvalues. At these points, called EPs (Kato 1976), the matrix is not diagonalisable since the eigenbasis is incomplete. Exceptional points are distinguished from a similar type of eigenvalue

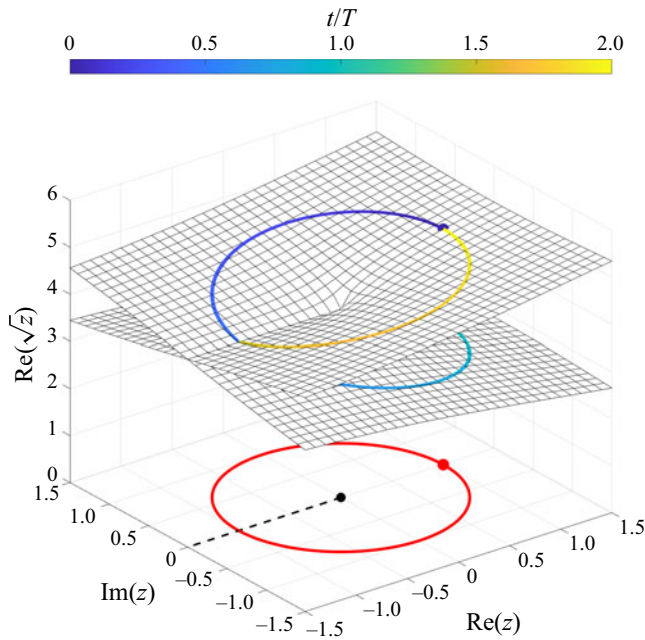


Figure 1. Sketch of the Riemann surface of the multivalued function  $f(z) = \sqrt{z}$  projected onto the three-dimensional space formed by the complex plane and  $\text{Re}(f(z))$ . The coloured line follows the analytic continuation of  $f$  applied to  $z_0 = \exp(2\pi i t/T)$  for  $t \in [0, 2T]$  where  $i$  is the imaginary unit and  $T$  is the period. The path of  $z_0$  is shown in red on the complex plane. The black dot marks the branch point  $z = 0$  and the dashed line indicates a branch cut. Note that the Riemann surface is shifted upwards to show the path on the complex plane.

degeneracy termed diabolic points (known as DP) in which the eigenvalues coalesce (cross) while the corresponding eigenvectors do not, thus maintaining diagonalisability (Miller 2017).

It can be shown that there are only a finite number of EPs in a given subset of the complex plane. If we are not at an EP, the number of eigenvalues  $s$  is independent of the parameters  $p$  and  $t$  and these depend smoothly on them (Kato 1976). The EPs are therefore crucial in determining the periodic orbits we are investigating.

The nature of EPs is in fact tightly linked to multivalued complex functions where solutions of the eigenvalue problem (2.2) as the parameters are varied constitute branches of analytic functions that have only algebraic singularities (Kato 1976) and the EPs are the branch points if such singularities exist. To illustrate the properties of multivalued functions, figure 1 shows a sketch of the real part of  $f(z) = \sqrt{z}$ . We see that following the trace of the unit circle (red) anticlockwise along the analytical continuation of  $f(z)$  around the branch point at the origin, the argument needs to complete two periods of the unit circle in order to return to the initial point on the Riemann sheet (blue dot). Note that the three-dimensional representation of  $f(z)$  is a projection (the imaginary part of the function value is not shown) and that the Riemann sheet is not intersecting itself in  $\mathbb{C}^2$ .

This means that circling an EP and returning to the same point in the complex plane may involve switching branches of the multivalued analytic function describing the trajectory. In fact, moving around an EP in the complex plane will lead to a cyclic permutation of period  $m$  of the analytic functions corresponding to the eigenvalues of  $A$  such that the analytic continuations revert to the same point after  $m$  revolutions. Note that  $m \geq 1$ , which



means that branch points must be EPs while the converse is not true since EPs can exist with  $m = 1$ , i.e. one can analytically continue the function around an EP returning to the same function value without requiring branch cuts (Kato 1976). Moreover, the merging of periodic orbits does not affect the instantaneous spectrum that is periodic for all  $t$ . The orbit merging therefore only manifests itself by tracking a specific eigenvalue over a period of  $t$ .

In terms of the eigenvalue trajectories  $\lambda_i(p, t)$  for non-normal matrices  $A$ , we conclude that they also form continuous periodic orbits that are mostly smooth but where the existence of EPs along the orbit may introduce kinks. At an EP, two (or more) eigenvalue orbits touch making the definition of the orbit locally ambiguous due to the collapse of the eigenspace dimensionality. Note that since EPs are rare and isolated, most eigenvalue trajectories will not cross an EP exactly thus circumventing ambiguity and forming smooth orbits.

In spite of its analyticity, the presence of EPs inside a closed orbit can lead to topological changes in the trajectory. If we follow any specific eigenvalue on a trajectory encircling an EP, we will return to the initial point (the same eigenstate) after  $m$  periods. With the emergence of eigenvalue permutation cycles due to the presence of the EP enclosed by the eigenvalue trajectory, the periodic orbits no longer necessarily have the same periodicity  $T$  as the parameter  $t$ . Instead, subharmonic orbits of period  $mT$  ( $m > 1$ ) can appear formed by the merging of  $m$  eigenvalue orbits into a permutation cycle. The parameters  $p$  can therefore be seen as control parameters in a bifurcation scenario where the critical value is associated with the crossing of an EP by an eigenvalue orbit. Varying a parameter past this critical value then leads to a topological change in the trajectories, i.e. the merging or breakup of the periodic orbits.

### 3. Pulsating Poiseuille flow

#### 3.1. Base flow

This work focuses on pulsating plane Poiseuille flow which refers to the flow between two infinite parallel plates induced by a time-periodic and spatially uniform axial pressure gradient. The resulting base flow has only a purely axial velocity component that is streamwise and spanwise independent and satisfies the incompressible Navier–Stokes equations in non-dimensional form that read

$$\left. \begin{aligned} \frac{\partial \mathbf{U}_b}{\partial t} &= -(\mathbf{U}_b \cdot \nabla) \mathbf{U}_b - \nabla p_b + \frac{1}{Re} \nabla^2 \mathbf{U}_b, \\ \nabla \cdot \mathbf{U}_b &= 0, \end{aligned} \right\} \quad (3.1)$$

where  $\mathbf{U}_b = (U_x(y, t), 0, 0)^T$  is the base flow velocity vector,  $p_b$  is the pressure and  $Re = U_c h / \nu$  is the Reynolds number based on the centreline velocity  $U_c$ , the channel half-height  $h$  and the kinematic viscosity  $\nu$ , supplemented by no slip boundary conditions at the channel walls.

We assume only pulsations at a single base frequency  $\Omega$  such that the time-periodic axial pressure gradient can be expanded in a Fourier series

$$-\frac{\partial p_b}{\partial x} = \sum_n G_x^{(n)} \exp(in\Omega t), \quad (3.2)$$

where  $G_x^{(n)} = 0$  for  $|n| > 1$ . Any other periodic signal can be analysed by retaining more terms in the Fourier series. In order to ensure that all physical quantities are real, we set  $G_x^{(-1)} = [G_x^{(1)}]^H$  where  $[\cdot]^H$  denotes complex conjugation.

Subharmonic eigenvalue orbits in pulsating Poiseuille flow

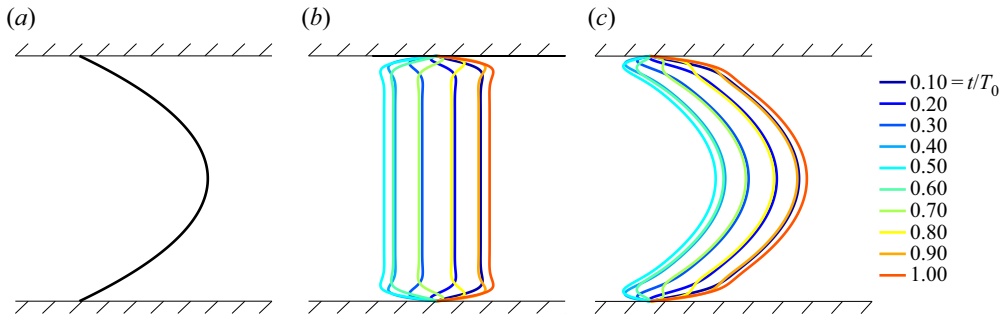


Figure 2. Schematic representation of the components of pulsating Poiseuille flow for  $\tilde{Q} = 0.6$  and  $Wo = 25$  over one period ( $T = 75.4$ ). The complete profile (c) is plane Poiseuille flow (a) superimposed with an oscillating flat Stokes layer (b).

The resulting axial velocity component has a similar structure and is given by

$$U_x(y, t) = \sum_n U_x^{(n)}(y) \exp(in\Omega t), \tag{3.3}$$

where  $U_x^{(n)} = 0$  for  $|n| > 1$  and the remaining terms are given by

$$U_x^{(n)}(\xi) = \begin{cases} \frac{G_x^{(n)} h^2}{v} \frac{i}{n Wo^2} \left( \frac{\cosh(\sqrt{i n} Wo \xi)}{\cosh(\sqrt{i n} Wo)} - 1 \right), & |n| = 1, \\ \frac{G_x^{(0)} h^2}{2v} (1 - \xi^2), & n = 0, \end{cases} \tag{3.4}$$

where  $\xi = y/h$ ,  $i$  is the imaginary unit,  $Wo$  is the Womersley number relating the channel half-height  $h$  to the thickness of the oscillating boundary layer  $\delta = \sqrt{\nu/\Omega}$  defined as

$$Wo = \frac{h}{\delta} = h\sqrt{\Omega/\nu} \tag{3.5}$$

and the steady component of the pressure gradient can be related to the corresponding centreline velocity of plane Poiseuille flow as

$$U_c = \frac{G_x^{(0)} h^2}{2v}. \tag{3.6}$$

Some further details can be found in Von Kerczek (1982) or Pier & Schmid (2017). Based on the Womersley and Reynolds numbers, the pulsation frequency can be computed as  $\Omega = Wo^2/Re$  which leads to a pulsation period of  $T = 2\pi Re/Wo^2$ . An example of the variation of the base flow profile for pulsating Poiseuille flow over one pulsation cycle is shown in figure 2.

A common measure for the oscillation amplitude is the fluctuating mass flow rate  $Q(t)$  which is given by the integral of the velocity over the channel width as

$$Q(t) = \sum_n Q^{(n)} \exp(in\Omega t) = \int_{-h}^{+h} U_x(y, t) dy. \tag{3.7}$$

After some manipulation we obtain the expressions for the components of  $Q(t)$  as

$$Q^{(n)} = \begin{cases} \frac{2G_x^{(n)} h^3}{\nu} \frac{i\gamma}{n Wo^2}, & |n| = 1, \\ \frac{2G_x^{(0)} h^3}{3\nu}, & n = 0, \end{cases} \quad (3.8)$$

with

$$\gamma = \frac{\tanh(\sqrt{i n} Wo)}{\sqrt{i n} Wo} - 1. \quad (3.9)$$

Following the notation in Pier & Schmid (2017, 2021) and Kern *et al.* (2021) to facilitate comparison, we express  $Q(t)$  as

$$Q(t) = Q^{(0)} \left( 1 + \tilde{Q} \cos(\Omega t) \right) \quad (3.10)$$

with the oscillation amplitude  $\tilde{Q}$  defined as

$$\tilde{Q} = \frac{Q^{(1)}}{2Q^{(0)}} \quad (3.11)$$

where we choose  $Q^{(n)}, \tilde{Q} \in \mathbb{R}$  for  $|n| \leq 1$  without loss of generality.

### 3.2. Orr–Sommerfeld operator

The classical approach for the stability analysis of the incompressible Navier–Stokes equations is to consider the linearised operator or Jacobian about a base flow. The linearised Navier–Stokes equations governing the evolution of an infinitesimal velocity perturbation  $\mathbf{u} = (u, v, w)$  with the associated pressure field  $p$  and external forcing  $f$  on top of a base flow  $U_b$  are given by

$$\left. \begin{aligned} \frac{\partial \mathbf{u}}{\partial t} &= -(U_b \cdot \nabla) \mathbf{u} - (\mathbf{u} \cdot \nabla) U_b - \nabla p + \frac{1}{Re} \nabla^2 \mathbf{u}, \\ \nabla \cdot \mathbf{u} &= 0, \end{aligned} \right\} \quad (3.12)$$

where the same non-dimensionalisation and boundary conditions as for the nonlinear equations are applied.

For parallel shear flows with a single inhomogeneous spatial direction such as pulsating Poiseuille flow, we can carry out a local stability analysis by Fourier transforming the problem in the streamwise direction yielding the wavenumber  $\alpha$ . The linearised equations (3.12) for a two-dimensional perturbation can then be written solely in terms of the wall-normal velocity  $\hat{v}(y, t)$  as

$$\mathcal{M} \frac{\partial \hat{v}}{\partial t} = \left( -i\alpha U_x \mathcal{M} - i\alpha U_x'' - \frac{1}{Re} \mathcal{M}^2 \right) \hat{v}, \quad (3.13)$$

where  $(\cdot)'$  denotes analytical differentiation in the inhomogeneous direction and the operator  $\mathcal{M} = k^2 - \mathcal{D}^2$  is given in terms of  $\mathcal{D}$ , the differential operator in the inhomogeneous direction.



This is the OS equation that can be conveniently recast in matrix form as

$$\frac{\partial \hat{v}}{\partial t} = \mathcal{L} \hat{v} \quad \text{with } \mathcal{L} := \mathcal{M}^{-1} \mathcal{L}_{OS}, \quad (3.14)$$

where  $\mathcal{L}_{OS}$  is the well known OS operator acting on the inhomogeneous direction ( $y$ ). Note that up to this point no assumption about the temporal behaviour of the perturbations is made.

The channel walls are no slip which leads to the Dirichlet boundary conditions at the wall given by

$$\hat{v} = \mathcal{D} \hat{v} = 0, \quad \text{at } y = \pm 1. \quad (3.15)$$

Note that three-dimensional perturbations can be studied in an analogous fashion via a Fourier transform in the spanwise direction and the inclusion of the evolution equation for the wall-normal vorticity with the appropriate boundary conditions. The resulting coupled OS–SQ equations have the same mathematical properties relevant to the analysis or EPs as the OS equation alone while being more expensive to solve. For this reason, as well as in an effort to reduce the parameter space of this study, we restrict our attention to the two-dimensional case. The differences to expect in the three-dimensional case, in particular with respect to the solution of the linear IVP, are discussed in the results section.

Assuming constant reference values for the steady centreline velocity  $U_c$  and the channel half-height  $h$  as well as the streamwise wavenumber  $\alpha$ , the operator  $\mathcal{L}$  can be expressed as an analytical function of the real parameters  $Re$  (or  $\nu$ ) encoding the relative importance of inertial and viscous effects,  $Wo$  (or  $\delta$ ) governing the relative importance of unsteady and viscous effects,  $\tilde{Q}$  describing the pulsation amplitude and time  $t$ . We can write

$$\mathcal{L} = f(Re, Wo, \tilde{Q}, t) \quad \text{with } Re, Wo, \tilde{Q}, t \in \mathbb{R}^+ \quad (3.16)$$

and we have

$$\mathcal{L}(t + T) = \mathcal{L}(t), \quad \forall t \in \mathbb{R}^+. \quad (3.17)$$

When the OS equation (3.14) is integrated in time starting from an initial condition  $\hat{v}_0$  at  $t = t_0$  we obtain a linear IVP

$$\frac{\partial \hat{v}}{\partial t} = \mathcal{L} \hat{v}, \quad \hat{v}(t_0) = \hat{v}_0, \quad t \in [t_0, \infty), \quad (3.18)$$

which leads to a solution which will experience transient, aperiodic behaviour before settling into a periodic motion as  $t \rightarrow \infty$ .

The remainder of this paper concerns the numerical analysis of the operator  $\mathcal{L}$  as well as the solution of the IVP (3.18). Details on the choice of spatial and temporal discretisations can be found in [Appendix A](#). This process leads to a discretised linear operator  $L$  that retains the parameter dependence of its continuous counterpart, in particular the analytic and periodic dependence on time.

#### 4. Exceptional points and subharmonic eigenvalue orbits

The properties described in § 2 then directly apply to the operator  $L$ . In particular, due to the strong non-normality of the OS operator (Trefethen *et al.* 1993) as well as the fact that we consider several independent parameters, we can expect the appearance of EPs in the temporal eigenvalue spectrum as we traverse the parameter space, in spite of the fact that earlier studies of plane Poiseuille flow failed to identify degeneracies in the

temporal problem (Koch 1986; Shanthini 1989). In contrast to these studies that did not consider pulsations, we set  $Re = 7500$  and  $\alpha = 1$ , which is slightly beyond the limit of linear stability of steady Poiseuille flow ( $Re_{crit} = 5772.22$  at  $\alpha = 1.02$  (Orszag 1971)) and focus on the variation of the pulsation frequency and amplitude and compare the results with the steady case. This choice reduces the parameter space to a manageable size, facilitates comparisons with the works of Pier & Schmid (2017) and Kern *et al.* (2021), that consider the same Reynolds number and streamwise wavenumber, while exhibiting interesting interactions between the pulsations and the intrinsic instability waves of Poiseuille flow. Section 5.4 revisits the choice of streamwise wavenumber and Reynolds number underlining the relevance and robustness of the results presented below.

#### 4.1. Identification of EPs and merging of eigenvalue orbits in the periodic OS spectrum

Before considering the evolution equation for the linearised problem, we first focus on the OS operator  $L$  itself to investigate whether EPs and subharmonic eigenvalue orbits occur in its spectrum.

For almost all parameter combinations  $p = (Re, Wo, \tilde{Q})$ , the eigenvalues do not exactly cross an EP during the pulsation ( $t \in [0, T]$ ) and their orbits therefore form continuous closed loops. The eigenvalue tracking is achieved using an *a posteriori* correlation analysis of subsequent eigenpairs using the function eigenshuffle (D’Errico 2021) while traversing the pulsation period in small steps. Unless stated otherwise, a time step of  $\Delta t = T/500$  was used which was found to be sufficient for the accurate tracking of the leading eigenvalues (in this work, the 50 leading eigenvalues were tracked containing a considerable part of the eigenvalues of the S-branch that do not join subharmonic orbits in the considered parameter range) and was reduced only in the close vicinity of EPs. In order to have consistent indexing of the spectra (and thus orbits) at different values of  $\tilde{Q}$ , the orbits are identified by tracking the eigenvalues in the same way while varying  $\tilde{Q}$  from 0 to the target amplitude and keeping the time constant at  $t = 0$ . Other indexing choices are possible but do not affect the results.

In order to find an EP, we begin with the steady OS spectrum, which corresponds to the periodic spectrum for  $\tilde{Q} = 0$ , and slowly increase the pulsation amplitude while monitoring the changes in the eigenvalue orbits. The EP can then be found as the point in the complex plane where two separate eigenvalue orbits touch during the period.

Figure 3 shows this process for two specific eigenvalues of the OS spectrum, marked A and B, together with the steady spectrum for reference. In order not to clutter the figure, only the orbits pertaining to these two eigenvalues are shown as the control parameter  $\tilde{Q}$  is increased. In figure 3(a) we see the evolution of the orbits starting with orbits at the base flow frequency around the steady value for  $\tilde{Q} = 0.05$ . These orbits progressively come closer to each other, coalesce at the EP (red cross) for  $\tilde{Q}_{crit} \approx 0.1341$  and subsequently form a subharmonic permutation cycle of period 2 that persists up until  $\tilde{Q} = 0.15$ . The merging of the loops is more clear in the close-up figure 3(b) where we see that while for  $\tilde{Q} < \tilde{Q}_{crit}$  all orbits form simple loops, once the amplitude passes  $\tilde{Q}_{crit}$ , the beginning of the orbit of eigenvalue A (full line, circle) connects to the orbit of eigenvalue B (dashed line, square) and *vice versa*. Note that to resolve the details of the orbit in the vicinity of the EP close to the critical amplitude, the local time step has to be decreased 200-fold to  $\Delta t = T/10^5$ .

To ascertain that we are dealing with an EP and not a diabolical point, we compute the angle  $\theta$  (in radians) between the eigenvectors  $\xi_A$  and  $\xi_B$  along each orbit, respectively,

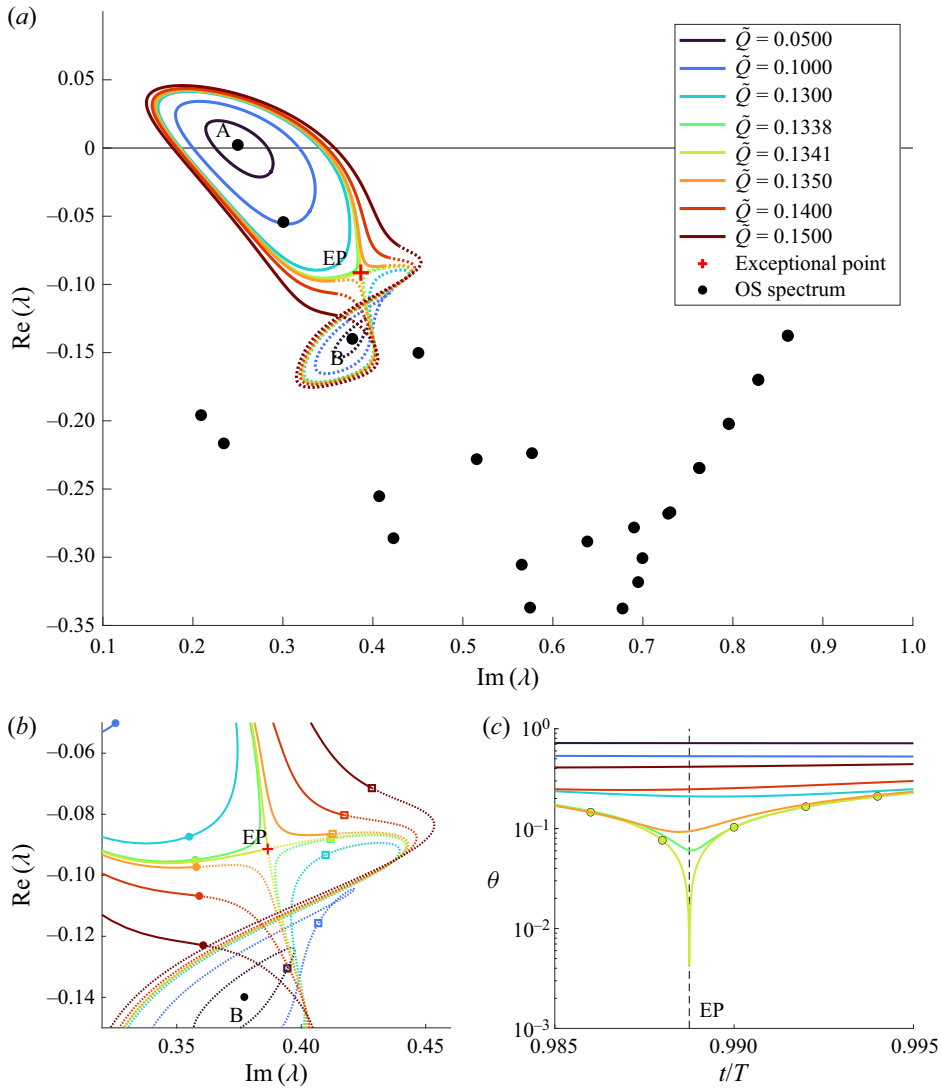


Figure 3. Variation of the periodic orbits of two eigenvalues and the angle between the corresponding eigenvectors as the pulsation amplitude  $\tilde{Q}$  is increased for the OS spectrum at  $Re = 7500$ ,  $Wo = 25$ . (a) Orbits corresponding to the eigenvalue A (full line) and B (dotted line) together with the steady OS spectrum (black dots). The EP where the orbits first touch and subsequently merge is marked by a red cross. (b) Close-up of (a) around the EP highlighting the merging of the orbits. The coloured circles and squares indicate the beginning of the corresponding cycle ( $t/T = 0$ ) relative to A and B, respectively. (c) Angle  $\theta$  (in radians) between the eigenvectors along the orbit showing the coalescence at the EP. The coloured dots indicate the time step used for regular runs that do not aim to locate the EPs precisely.

which is given by

$$\cos \theta = \frac{\langle \xi_A, \xi_B \rangle_E}{\|\xi_A\| \|\xi_B\|}, \quad \text{with } \|\xi_i\| = \sqrt{\langle \xi_i, \xi_i \rangle_E}, \quad (4.1)$$

where the inner product  $\langle \cdot, \cdot \rangle_E$  is the energy norm that arises naturally from the OS–SQ equations (Schmid 2007) and reads

$$\langle \xi_A, \xi_B \rangle_E = \frac{1}{2k^2} \int_{-1}^1 \xi_A^H M \xi_B \, dy, \quad (4.2)$$

where  $(\cdot)^H$  denotes complex conjugation and  $M$  is the discretised version of the mass matrix  $\mathcal{M}$ .

Following the angle  $\theta$  along the orbit as shown in figure 3(c), we observe that as we come closer to  $\tilde{Q}_{crit}$ , the angle  $\theta$  progressively decreases close to the EP to then abruptly vanish exactly at the EP indicating the coalescence of both eigenvalue and eigenvector typical for EPs. Once passed  $\tilde{Q}_{crit}$ , the angle increases again to values similar to before the coalescence. The abruptness of the coalescence is an indication of the well known sensitivity of the eigenstates close to an EP (Or 1991; Heiss 2012). This has the practical advantage that the orbits can be traced with comparatively large steps in  $t$  since the variation of the eigenstates is slow unless an orbit passes very close to an EP where a refinement is advisable in order to resolve the details of the orbit. Furthermore, the amplitude range for which the orbit variation is extreme is a narrow band around  $\tilde{Q}_{crit}$ . The coloured dots in figure 3(c) indicate the time step  $\Delta t = T/500$  used in this work with which the location of the EP cannot be determined accurately but at the same time unambiguous eigenvalue tracking is ensured since the eigenvalues are extremely unlikely come too close to the point of coalescence.

#### 4.2. Variation of the subharmonic orbits with the pulsation frequency and amplitude

The next step in understanding the subharmonic eigenvalue orbits is to analyse their prevalence in the parameter space. We consider the parameter ranges  $Wo \in [0.1, 150]$  and  $\tilde{Q} \in [0, 0.6]$ , track the eigenvalue loops over a period and count the number of eigenvalues that form permutation cycles. Due to the symmetry in the base flow, the OS operator has both symmetric (varicose) and antisymmetric (sinuous) eigenpairs. Since EPs require coalescence of eigenstates, they can only occur within their respective symmetry groups. For the remainder of the analysis, we will present symmetric and antisymmetric modes separately. For completeness, the link between the subharmonic eigenvalue orbits in the spectrum of the OS operator and their appearance in the spectrum of the reduced operator obtained using the OTD modes is described in Appendix A.

The appearance of subharmonic orbits as a function of  $Wo$  and  $\tilde{Q}$  is presented in figure 4. Figure 4(a) gives an overview over the total number of subharmonic orbits in the considered parameter range and figure 4(b,c) highlight the length of subharmonic orbits that involve the dominant symmetric and antisymmetric eigenvalues, which are the only eigenvalues that exhibit positive growth rates across a pulsation cycle. Their location in the steady spectrum is shown in the inset in figure 4(a) for reference. We denote by  $m$  the length of a given subharmonic orbit (i.e. the number of eigenvalues it contains) and by  $k_{sub}$  the number of subharmonic permutation cycles ( $m > 1$ ) that exists for a specific parameter setting.

We see that for a broad range of pulsation frequencies ( $5 \leq Wo \leq 90$ ), subharmonic eigenvalue orbits are very common as the pulsation amplitude increases, starting as early as  $\tilde{Q} = 0.07$  at  $Wo = 18$ . Beyond this range, the subharmonic cycles appear at progressively higher amplitudes until, both for very low ( $Wo = 0.1$ ) and very high ( $Wo = 150$ ) pulsation frequencies, no subharmonic eigenvalue orbits are detected at all in the considered amplitude range. Based on the distributions in figure 4, it is to be expected that the range of

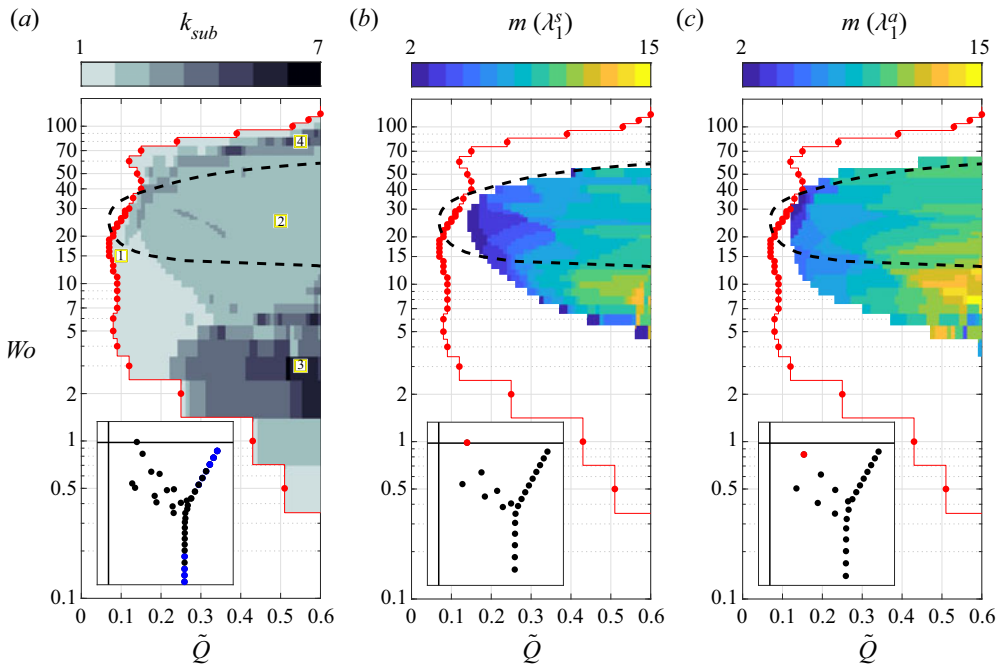


Figure 4. Plots of the appearance of subharmonic eigenvalue orbits as functions of  $Wo$  and  $\tilde{Q}$  (in steps of 0.01) at  $Re = 7500$ . The red line in all plots indicates the limit  $k_{sub} \geq 1$  (if any) for each considered Womersley number (red dots). The dashed line indicates the neutral curve based on Floquet stability analysis. (a) Total number of distinct subharmonic orbits. The inset shows a sketch of the steady full OS spectrum. The eigenvalues marked in blue never form subharmonic orbits in the considered parameter range. Note that the eigenvalues along the P-branch come in pairs in close proximity that cannot be distinguished in this plot. For the numbered parameter combinations marked with yellow squares in (a) the full eigenvalue orbits are shown in the corresponding row in figure 5. (b) Subharmonic orbits including the dominant symmetric eigenvalue (marked red in the inset spectrum) coloured by the period  $m$  (in multiples of the base period  $T$ ). (c) Same as (b) but for the dominant antisymmetric eigenvalue (marked red in the inset spectrum).

pulsation frequencies that support subharmonic eigenvalue orbits will continue to widen as the pulsation amplitude is increased beyond  $\tilde{Q} = 0.6$ . Following the classification of the eigenvalues into the three branches A, P and S according to their location in the spectrum proposed by Mack (1976), we observe that the permutation cycles mostly start with eigenvalues located at the intersection of the three branches of the spectrum but quickly spread to include most eigenvalues of the A-branch. Only the outermost modes of the P-branch and very damped eigenvalues of the S-branch (marked in blue in the inset in figure 4a) maintain isolated orbits with the base flow frequency in the entire considered parameter range.

In figure 4(a), within the region where subharmonic eigenvalue orbits occur, we can further distinguish two parameter ranges with very different behaviour.

For intermediate pulsation frequencies (roughly  $10 \leq Wo \leq 60$ ), only one or two permutation cycles form. The lengths of these cycles grow quickly as the pulsation amplitude increases and they eventually contain up to  $m = 15$  eigenvalues ( $Wo = 8$  at  $\tilde{Q} = 0.6$ ). This is also the only region in which  $\lambda_1$  and  $\lambda_4$  eventually join the cycles and thus the dominant eigenvalues with temporarily positive growth rates are part of subharmonic orbits.

For pulsation frequencies below approximately  $Wo = 9$  or beyond  $Wo = 60$ , instead of two large subharmonic orbits, we observe the emergence of up to seven distinct permutation cycles and the orbits of  $\lambda_1$  and  $\lambda_4$  merge, if at all, only for high pulsation amplitudes. Finally, for  $6 \leq Wo \leq 10$ , there is also a sharp increase in the number of distinct subharmonic orbits as the pulsation amplitude increases beyond  $\tilde{Q} = 0.55$ , which coincides with a drastic reduction of the number of eigenvalues in  $\varphi_1$  (figure 4b) indicating that the large orbit has disintegrated into a number of separate, shorter orbits.

In order to understand the effect of the pulsation frequency and amplitude on the formation of permutation cycles, it is instructive to consider the location of the orbits in the complex plane. In figure 5 each row shows all the eigenvalue orbits for one of the four numbered cases marked with yellow squares in figure 4(a) that highlight prominent features. In the following discussion we will denote by  $\varphi^s$  and  $\varphi^a$  the permutation cycles formed by symmetric and antisymmetric eigenvalues, respectively. The orbits in each figure are indexed by increasing stability.

Figure 5(a,b) shows a typical case at moderate pulsation frequency ( $Wo = 15$ ) where the amplitude  $\tilde{Q}$  has crossed the critical threshold and the first subharmonic eigenvalue orbit (involving two antisymmetric modes) has appeared close to the intersection of the eigenvalue branches. We also observe the characteristic feature that the orbits corresponding to eigenvalues of the A-branch experience more pronounced excursions over a cycle, especially in terms of growth rate, than those of the P- and S-branches. The latter, instead, vary mainly along the imaginary axis, following the variation of the mass flow rate which can be seen from the fact that the eigenvalues have the largest (smallest) imaginary part at  $t/T = 0$  ( $t/T = 0.5$ ) where  $Q(t)$  is maximal (minimal), the former marked by a filled dot along each orbit.

As the pulsation amplitude is increased, the subharmonic orbits expand and eventually encompass all eigenvalues of the A-branch, separated into two distinct permutation cycles based on their symmetry. Figure 5(e,f) show an example of this situation at  $Wo = 25$  and  $\tilde{Q} = 0.5$ . Although the details of the orbits, especially for eigenvalues on the A-branch, vary considerably, all cases at intermediate pulsation frequencies are structurally similar to the case presented here featuring only two permutation cycles. Note that for this parameter combination, both  $\varphi_1^s$  and  $\varphi_1^a$  exhibit positive growth rates over part of the cycle.

For higher pulsation frequencies, the variation in the growth rate of the eigenvalues across the cycle reduces. Eventually, the orbits of  $\lambda_1$  and  $\lambda_4$ , being relatively isolated in the spectrum, no longer merge into subharmonic orbits even at high pulsation amplitudes as shown in figure 5(g,h) for  $Wo = 80$  and  $\tilde{Q} = 0.55$ . Nevertheless, the eigenvalues close to the intersection of the branches continue to form permutation cycles and exhibit complex orbits.

If we instead reduce the pulsation frequency, we see a smaller growth rate variation only for  $\lambda_1$  and  $\lambda_4$  while other eigenvalues from the A-branch and the intersection area exhibit strong variations in both real and imaginary parts across the cycle. Moreover, in this part of the parameter space, the leading eigenvalues do not form subharmonic orbits. It can also be noted that, unlike all cases at intermediate and high pulsation frequencies, the roughly oval orbits on the A- and P-branches at low Womersley numbers are tilted with the major axes pointing towards the origin of the complex plane.

The smooth orbits formed by the eigenvalue traces over a period are accompanied by the corresponding eigenvectors through the permutation cycle. The variation of the eigenvector of  $\varphi_1^s$  over a complete subharmonic cycle is shown in movie 1 of the supplementary material available at <https://doi.org/10.1017/jfm.2022.515> for  $Wo = 25$ ,  $\tilde{Q} = 0.2$  where  $\varphi_1^s$  has a period of  $m = 3$ .



Subharmonic eigenvalue orbits in pulsating Poiseuille flow

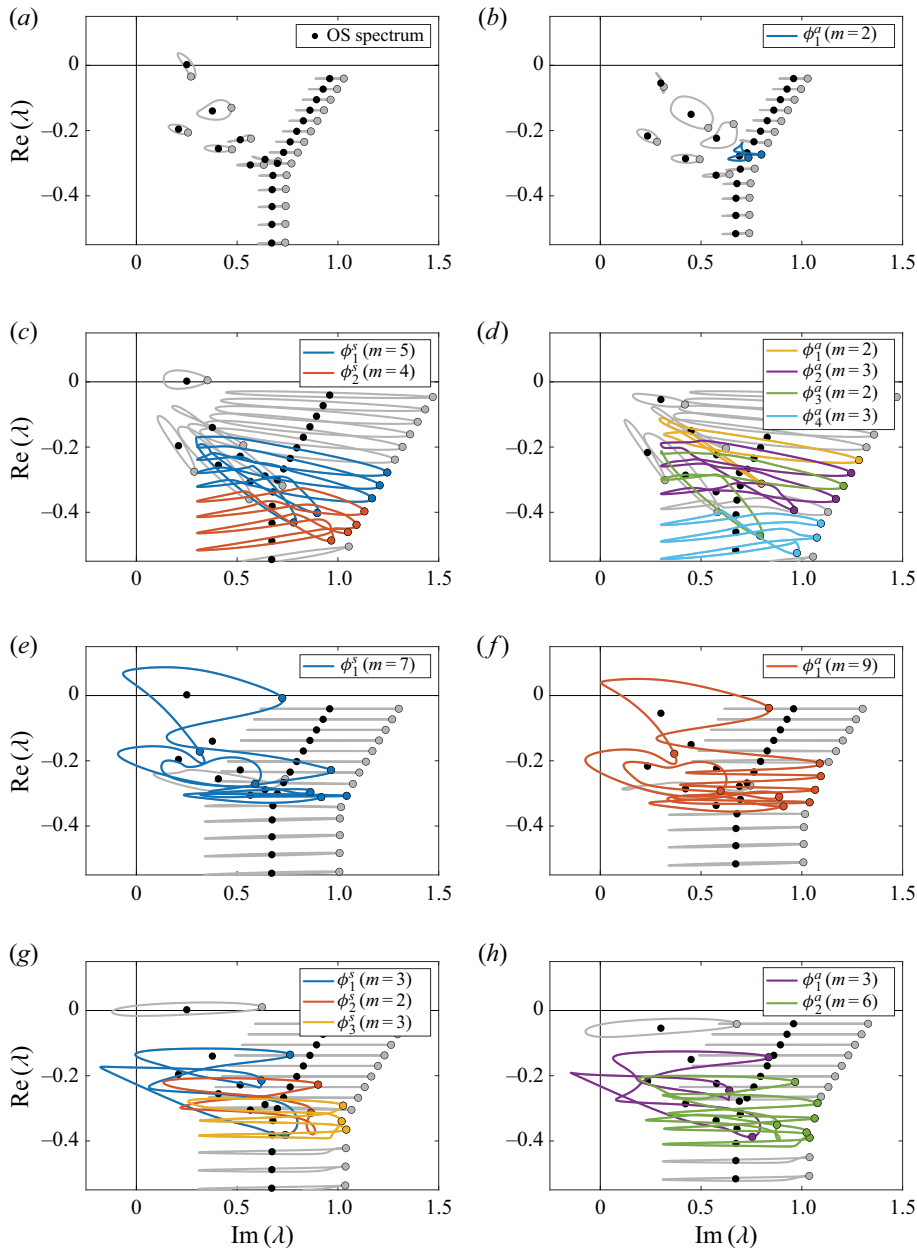


Figure 5. Eigenvalue orbits ((a,c,e,g) symmetric; (b,d,f,h) antisymmetric) at  $Re = 7500$  for four representative combinations of  $Wo$  and  $\tilde{Q}$  marked by yellow squares in figure 4(a) showing the variations possible in the parameter space. If present, the subharmonic orbits  $\phi_i^s$  and  $\phi_i^a$  are highlighted in colour. The black dots indicate the OS spectrum and the coloured dots the eigenvalue loci at the beginning of each period of  $t$ . Here (a,b)  $Wo = 15$ ,  $\tilde{Q} = 0.1$ ; (c,d)  $Wo = 3$ ,  $\tilde{Q} = 0.55$ ; (e,f)  $Wo = 25$ ,  $\tilde{Q} = 0.5$ ; (g,h)  $Wo = 80$ ,  $\tilde{Q} = 0.55$ .

Within the parameter range considered in this work, the cases in which  $\lambda_1$  eventually joins a subharmonic eigenvalue orbit are particularly interesting because the variation of the instantaneous operator spectrum has a large impact on the evolution of a linear perturbation. We will analyse the periodic orbits for three Womersley numbers in detail,

---

$Wo$	0.1	1	5	25	50	150	300
$\mathcal{T}$	$1.3 \times 10^{-6}$	$1.3 \times 10^{-4}$	$3.3 \times 10^{-3}$	0.083	0.33	3.0	12

---

Table 1. Overview of the range of time scale ratios of the viscous time scale and the pulsation time scale as a function of the Womersley number for  $Re = 7500$ .

namely  $Wo = 10, 18$  and  $25$ , that span the range of pulsation frequencies of interest and exhibit very different behaviour as the pulsation amplitude is varied.

### 4.3. Time scale analysis

The qualitative differences in the spectra and hence the periodic eigenvalue orbits for different pulsation frequencies can be understood by comparing the time scale of the intrinsic instabilities of Poiseuille flow and the pulsation frequency.

Following the classical time scale analysis for parallel shear flow with considerable mean flow described in Davis (1976), the relevant time scale ratio between the principal viscous flow time scale and the pulsation time scale becomes

$$\mathcal{T} = \frac{2\beta^2}{Re} = \frac{Wo^2}{Re}, \tag{4.3}$$

where we note that, due to differing normalisations, the Womersley number  $Wo$  and the frequency parameter  $\beta$  (not to be confused with the spanwise wavenumber traditionally using the same symbol) are related as

$$\frac{\beta}{Wo} = \sqrt{2}. \tag{4.4}$$

An overview of the values of  $\mathcal{T}$  for different values of the Womersley number including the range considered in this work, assuming a constant Reynolds number of  $Re = 7500$ , are given in table 1.

It is clear that for two different pulsation frequencies at the same Reynolds number, the time scale ratios  $\mathcal{T}$  cannot be directly compared since the Womersley number affects both the pulsation time scale and the velocity profile. A more rigorous assessment of the separation of scales and the role of the Reynolds number can be made via a Wentzel–Kramers–Brillouin–Jeffreys (WKBJ) analysis in time (see Benney & Rosenblat 1964) but this analysis is outside of the scope of this work that focuses on the variation of the pulsation parameters  $Wo$  and  $\tilde{Q}$ . For our purposes focusing on the emergence of subharmonic eigenvalue orbits it is sufficient to analyse the behaviour for extreme values of the pulsation frequency. We consider two cases in particular, namely  $Wo \ll 1$  ( $\mathcal{T} \ll 1$ ) and  $Wo \gg 1$  such that  $\mathcal{T} \gg 1$  for which the variation of the base flow profiles and corresponding eigenorbits over the pulsation cycle at  $\tilde{Q} = 0.5$  are shown in figure 6.

We see from the definition that the time scale separation between viscous effects and the base flow pulsation scales with the square of the Womersley number and approaches zero for the lowest pulsation scales considered in this work, indicating that the flow in that parameter region is quasi-steady (QS), i.e. the pulsation period is so long that the flow can essentially adapt instantaneously to the changes in pressure gradient. The flow therefore behaves instantaneously like plane Poiseuille flow with a parabolic velocity profile, the pulsations only varying the effective Reynolds number. The corresponding periodic orbits

## Subharmonic eigenvalue orbits in pulsating Poiseuille flow

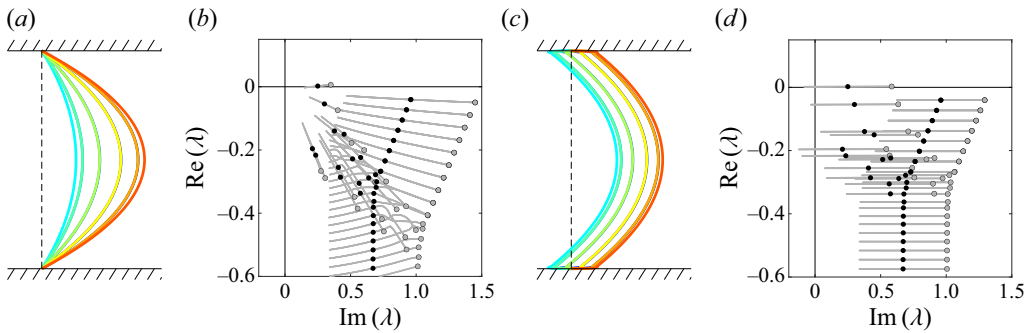


Figure 6. Base flow profiles and corresponding eigenorbits for extreme values of the Womersley number at  $\tilde{Q} = 0.5$ . In this parameter range there are no subharmonic eigenvalue orbits. Here (a,b)  $Wo = 0.1$ ; (c,d)  $Wo = 300$ .

have the base flow frequency and do not show any hysteresis over the cycle, i.e. there is no difference between the base flow acceleration and deceleration phases.

At the other extreme of the  $Wo$ -spectrum, for  $\mathcal{T} \gg 1$ , the pulsation cycles are so short compared with the viscous time scale that the flow does not have time to adapt at all and the velocity fluctuation induced by the varying pressure gradient and superimposed on the steady parabolic component increasingly resembles a top hat profile. The resulting base flow profile exhibits extremely thin oscillating boundary layers close to the walls but has an otherwise constant wall-normal variation that is translated along the streamwise direction during a pulsation cycle. In this regime, the orbits have the base flow frequency, exhibit no hysteresis and only oscillate along the imaginary axis synchronised with the pulsations. In fact, the second derivative of the base flow profile in the wall-normal direction, pivotal for its stability characteristics, is constant and equal to that of the steady Poiseuille flow everywhere with the exception of the oscillating boundary layer that is too thin to noticeably affect the instability waves since the inflection points are located too close to the wall (Kern *et al.* 2021).

The result that pulsations do not lead to an increased instability of the base flow profile for high pulsation frequencies is in line with the conclusions drawn in Davis (1976) with regard to the stability of highly inflectional Stokes layers that are dynamically similar for  $\delta \ll h$  and are found to be unstable only for small pulsation frequencies. For pulsating Poiseuille flow, however, the results do not extend to very low frequencies ( $Wo \ll 1$ ) since the comparison breaks down when the two Stokes layers merge at the centreline when  $\delta \approx h$  and the base flow profile ceases to be inflectional.

From the time scale analysis we conclude that, while for intermediate values of  $Wo$  the time scales associated with the base flow pulsation and viscous effects are similar and we thus see considerable variation of the stability characteristics with the Womersley number, the flow at very high (very low) pulsation frequencies only depends on the (effective) Reynolds number and we do not find any subharmonic eigenvalue orbits.

### 4.4. Pulsations and non-normal growth potential

In view of the considerable non-normality of the OS operator, the spectrum itself only paints only part of the picture. In order to fully examine the stability characteristics of the operator, it is crucial to consider the energy growth potential brought about by the superposition of non-orthogonal eigendirections with very different growth rates that can lead to large transient amplification of disturbances even in linearly stable flows (Reddy &

Henningson 1993; Trefethen *et al.* 1993). Of particular interest in the context of pulsating Poiseuille flow is the question how the non-normal growth potential, intrinsic to plane Poiseuille flow, is altered by the addition of a pulsatile component to the base flow. A common measure of this potential is the numerical abscissa of the operator, often denoted  $\sigma_{max}$ , which encodes the maximum instantaneous growth rate possible taking into account both modal and non-modal mechanisms (Trefethen & Embree 2005; Schmid 2007). The numerical abscissa of a matrix  $L$  is given by the largest eigenvalue of its Hermitian part, i.e. we have

$$\sigma_{max} = \lambda_{max} \left( \frac{1}{2} (L + L^H) \right), \tag{4.5}$$

where  $(\cdot)^H$  denotes complex conjugation, and can also be computed as the maximum protrusion of the numerical range into the unstable half-plane (Trefethen 1997).

In a recent study of the stability of pulsating Poiseuille flow, Kern *et al.* (2021) have conjectured that, in spite of the considerable variation of the instantaneous eigenvalues over a cycle, the pulsations only have a negligible impact on the full non-normal growth potential. Due to the high computational cost of the method used in the study when aiming to capture the full non-normality of the operator, the impact of the pulsations on the non-modal growth potential was analysed only for the case  $Wo = 25$  and  $\tilde{Q} = 0.2$  where the numerical abscissa was found to fluctuate within 1 % of the corresponding steady value ( $Re = 7500, \tilde{Q} = 0$ ) during the pulsation cycle.

Using the full operator from the local analysis, we can efficiently map the effect of pulsations on the numerical abscissa and test the conjecture over the full parameter range. In addition to the absolute value of  $\sigma_{max}$  we will also consider  $\Delta\sigma = \sigma_{max} - \sigma_r$ , the fluctuation of the numerical abscissa with respect to the steady reference value  $\sigma_r$ , which is particularly useful for harmonic variations around the reference value. Based on the time scale analysis above, we can begin by defining the extremal values for the numerical range. For very large values of  $Wo$ , the numerical abscissa is equal to the steady value, i.e.  $\Delta\sigma = 0$ , since the spectrum is only translated along the imaginary axis. For very low pulsation frequencies, on the other hand, we are in the QS regime and the base flow profile  $U_{QS}(t)$  is parabolic and synchronised with the fluctuating mass flow rate, such that

$$U_{QS}(t) = \frac{3}{2} \frac{Q(t)}{2h} (1 - \xi^2), \tag{4.6}$$

where we have used the steady state relationship  $Q = U_b 2h = \frac{2}{3} U_c 2h$  with  $U_b$  the bulk velocity.

It is clear that the flow rate variations in the QS regime are equivalent to a variation of the Reynolds number in plane Poiseuille flow such that the numerical abscissa can be computed from the corresponding steady problem at each instant in the pulsation cycle. Therefore, the variation of the non-normal growth potential in the two extreme cases relies solely on the intrinsic non-normal growth mechanisms of steady Poiseuille flow. In the following, we will compare the corresponding profiles for the numerical abscissa with the data for intermediate pulsation frequencies.

The variation of the numerical abscissa for pulsating Poiseuille flow over the full range of pulsation frequencies and amplitudes considered in this work is shown in figure 7 compared with the QS limit (black dashed line). The first observation is that the relatively simple dependence of the numerical abscissa on the pulsation frequency and amplitude that is similar over the entire considered parameter range. This is in stark contrast with the complex behaviour of other spectral quantities such as the instantaneous eigenvalues

## Subharmonic eigenvalue orbits in pulsating Poiseuille flow

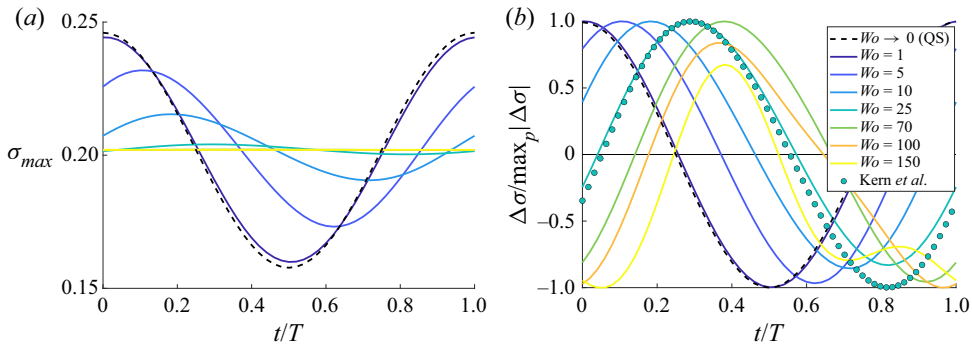


Figure 7. Variation of the numerical abscissa  $\sigma_{max}$  of the OS operator for pulsating Poiseuille flow at  $Re = 7500$  and  $(\alpha, \beta) = (1, 0)$  as a function of time and the pulsation frequency and amplitude. (a) Variation of the numerical abscissa over the pulsation cycle for different pulsation frequencies for  $\hat{Q} = 0.2$  compared with the variation in the QS limit (dashed line). (b) Same data as in (a) but presenting  $\Delta\sigma$  normalised by the maximum deviation from the steady value over the period to highlight the intracyclic variation at different frequencies. The dots correspond to the data from Kern *et al.* (2021) using  $r = 100$  modes (cf. figure 10 in Kern *et al.* (2021)) for the same case.

(compare with the large variability of the eigenvalue orbits within the parameter range in figure 5) or the Floquet exponents (especially at low pulsation frequencies where the variation of the intercycle stability is high non-monotonic, see Pier & Schmid (2017) and Kern *et al.* (2021)). Not only are the slopes of  $\max_p |\Delta\sigma|$  similar, also the intracyclic variations of the numerical abscissa are highly regular for all but the highest pulsation frequencies which have negligible amplitude. The similarity of the intracyclic variation across the parameter range to the QS limit further supports the conclusion that the main mechanism generating it is the same. The comparison with the data from Kern *et al.* (2021) shows very good agreement, in particular in terms of the intracyclic variation. The amplitude mismatch is minute considering that the corresponding amplitude  $\max_p |\Delta\sigma|$  is around 1 %  $\sigma_r$  and shows that the computation indeed captured nearly the fully non-normal growth potential.

The orderly variation of the numerical abscissa across the considered parameter range is all the more surprising given the fact that is uncorrelated with the leading eigenvalues of the Jacobian, both in terms of intracyclic variation and in amplitude. It is especially striking that we do not see any trace of the EPs that are so abundant in the spectrum and are characterised by eigenvector coalescence and thus lead to highly non-orthogonal eigenvectors in their vicinity. There are two explanations for this fact. Firstly, for non-normal growth to occur involving two non-orthogonal eigendirections, it is not sufficient for them to be nearly colinear but they also require very different growth rates. Since the coalescing eigenvectors, instead, have more similar growth rates the closer they come to the EP, they cannot, by themselves, generate considerable non-normal growth. Secondly, the non-modal growth mechanisms intrinsic to plane Poiseuille flow that lead to the maximum transient growth rely on very damped modes. In particular,  $r = 100$  real modes (which corresponds to 50 complex modes) are necessary to map the full potential which includes modes from the S-branch that are considerably less affected by the pulsation than the modes from the A-branch that predominantly form the permutations cycles. These modes in fact exhibit a harmonic variation over the pulsation cycle and exhibit considerable growth rate variations only for low values of the Womersley numbers where the flow is close to the QS regime (compare the most damped modes in figure 5) which is in line with the behaviour of the numerical abscissa.

Based on these analyses, the conjecture that the addition of a pulsatile component does not considerably alter the perturbations having the maximum non-normal growth potential in two-dimensional Poiseuille flow can be confirmed. The intracyclic variations of the numerical abscissa over the full range of Womersley numbers, not only in the limiting cases, are caused by the mechanisms intrinsic to plane Poiseuille flow that dependent on the effective Reynolds number instead of the details of the oscillating base flow profile. The mechanisms that are dependent on the modes that experience modulation due to the pulsations lead to smaller non-normal growth and therefore have no repercussion on the numerical abscissa.

This conclusion is in line with results from the recent work by Pier & Schmid (2021) where the authors computed the optimal transient growth curves for two- and three-dimensional disturbances in pulsating Poiseuille flow that showed the universality of the Orr mechanism and the lift-up effect in optimal non-modal growth known from steady Poiseuille flow also in the pulsating case. The study found that for pulsating Poiseuille flow the largest transient growth is achieved either via the lift-up effect like in the steady case for low pulsation amplitudes (largely independent of the frequency) or, as the pulsation amplitude increases, via the Orr mechanism. The two-dimensional mechanism takes over as the driver for maximum energy growth since the perturbation first grows via the Orr mechanism just before the phase of linear instability where it switches gears and takes advantage of the modal growth of the unstable eigenvalue that increases exponentially with the pulsation amplitude. The analysis of the numerical abscissa shows that non-normal growth in pulsating Poiseuille flow is fundamentally similar to the steady counterpart not only for the optimal initial condition but also for the instantaneously most amplified structure.

## 5. The linear periodic IVP

The emergence of the subharmonic eigenvalue orbits as the pulsation amplitude is increased changes the topology of the spectrum across the perturbation cycle which also affects the linear evolution of a perturbation.

To analyse the impact of the changes to the instantaneous spectrum on the evolution of a linear perturbation in the periodic regime, we integrate (3.18) in time and compare the evolution of the perturbation with the eigenspectrum of  $L$ . To avoid numerical overflow or underflow, we continuously normalise the perturbation  $v$  to unit energy, i.e. at the beginning of every time step we have

$$E(q) = \langle v, v \rangle_E = 1. \tag{5.1}$$

The periodic solution of the IVP is independent of the initial conditions when the transients have passed. We could therefore initialise the computations with noise but in order to speed up the convergence to the periodic solution and to facilitate reproduction, we choose a specific initial condition. In particular, we set

$$v_0 = \xi_{max}(t_0) \quad \text{with } t_0 = 0, \tag{5.2}$$

where  $\xi_{max}$  denotes the instantaneous eigenvector of  $L$  corresponding to the eigenvalue which reaches the maximum growth rate over the cycle (usually  $\lambda_1$ ). The initial time  $t = 0$  corresponds to the instant when  $Q(t)$  reaches its maximum.

Once the perturbation has settled into a periodic orbit, we record its growth rate. The instantaneous growth rate  $\gamma$  of the perturbation from  $v^n$  at time step  $t^n$  to  $v^{n+1}$  at time step



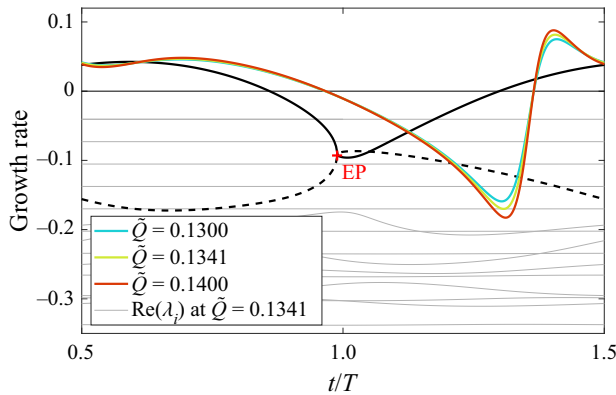


Figure 8. Instantaneous perturbation growth rates for three configurations from figure 3 close to  $\tilde{Q}_{crit}$  over one period after the transients have passed. The grey lines indicate the instantaneous symmetric spectrum at  $\tilde{Q}_{crit}$  and the eigenvalue orbits merging at the EP (marked with a red cross) are highlighted in black (solid and dashed). The colour coding for the IVP solutions is the same as for the corresponding spectra in figure 3.

$t^{n+1}$  separated by  $\Delta t$  is given by

$$\gamma = \frac{1}{\sqrt{E(v^n)}} \frac{\sqrt{E(v^{n+1})} - \sqrt{E(v^n)}}{\Delta t} = \frac{\sqrt{E(v^{n+1})} - 1}{\Delta t} \quad (5.3)$$

due to the normalisation of the energy at each step. This instantaneous growth rate is then compared with the eigenvalue orbits discussed above.

### 5.1. Effect of EPs on the linear IVP

The first question of interest regarding the solution of the IVP in the context of EPs is which effect the eigenvalue degeneracies have directly on the linear solution and, in particular, what happens to the solution close to a degeneracy. In our study, we have not been able to detect any abrupt or notable changes in the instantaneous linear solutions as the pulsation amplitude is increased past a bifurcation point where an EP occurs during the period. As a typical example, we consider the same case as for the identification of the EPs (figure 3, i.e.  $Wo = 25$ ) and compare the linear solutions computed for three different pulsation amplitudes around the critical value at which the EP forms. It turns out that the linear growth rates, shown in figure 8, behave nearly identically both before, after and very close to the bifurcation point. This is not particularly surprising considering the ubiquity of EPs we have documented together with the facts that in steady flows energy growth varies smoothly (channel flow (Reddy & Henningson 1993)) and spectral degeneracies have been studied previously without uncovering traces of dramatic growth variations for nearly degenerate operators (Gustavsson & Hultgren 1980; Koch 1986; Shanthini 1989). Note that the operator is never exactly degenerate numerically.

### 5.2. Branch transition on subharmonic eigenvalue orbits

Although the EPs themselves do not seem to leave any traces in the evolution of a linear perturbation, they have a pronounced effect via the formation of subharmonic eigenvalue orbits.

The evolution of the linear perturbation, at each instant in time, is dictated by the instantaneous spectrum of the OS operator. Since the operator changes continuously,

the perturbation never fully aligns with the dominant eigendirection for long times as we would expect in the steady case. Nevertheless, the perturbation, so long as it has a projection on an instantaneous eigendirection, will grow in that direction and preferentially towards the dominant eigenstate. Two major factors governing this alignment are therefore the rate at which the eigenstates change compared with their instantaneous growth rates and the difference between the growth rates of the dominant and subdominant eigenstates with a considerable projection on the instantaneous perturbation.

This imperfect alignment with the dominant eigendirection can be seen in [figure 9](#) comparing the instantaneous growth rates of the linear solution with the corresponding symmetric spectrum (only the symmetric spectrum is shown since the linear perturbation is always symmetric in the periodic regime and therefore the asymmetric modes are irrelevant) for a wide range of pulsation frequencies and amplitudes. The alignment is best when the eigenstates only change slowly (typically, a slow variation of the growth rate is linked to a slow variation of the eigenvector for shown here) and the dominant eigenvalue grows much faster than the subdominant, such as during the amplification phase at low pulsation frequencies (column 3). On the other hand, the alignment is less pronounced at higher pulsation frequencies where the operator changes quickly (column 1) as well as during the damping phases where dominant and subdominant eigenvalues exhibit similar growth rates. In these regions we also see considerable growth rate overshoots/undershoots and wiggles. These wiggles, although they already appear earlier, become particularly pronounced once the dominant eigenvalue forms a subharmonic orbit (see [figure 9d,e,i](#)) and are linked to the transition of the linear perturbation from the decaying branch to the amplified branch of the eigenvalue orbit. The branch transition is necessary because, as we know from Floquet theory, the linear perturbation eventually settles into a periodic motion at the same frequency as the base flow once the initial transients have passed. As the branch transition happens during a part of the cycle where the spectrum is heavily damped and the perturbation is influenced by several non-orthogonal decaying eigendirections at the same time, it is likely that the wiggles are due to non-normal growth bursts. For very large pulsation amplitudes, the wiggles are suppressed and the branch transition is increasingly abrupt (see [figure 9j-k](#)).

We know that the non-normal growth mechanisms from plane Poiseuille flow and hence their time scales are essentially unchanged when pulsations are added both instantaneously (see §4.4) and when considering optimal disturbances (Pier & Schmid 2021). It is therefore useful to compare the time scale of the growth bursts we observe in the periodic regime with that of the Orr mechanism, central to optimal transient growth of two-dimensional disturbances. Considering the IVP for plane Poiseuille flow, the optimal initial condition for maximum transient growth at  $Re = 7500$  with  $\alpha = 1$  (close to the transiently most amplified streamwise wavenumber) reaches the maximum energy at  $t_{Orr} = 27t_U$  with the mean flow advection time scale  $t_U = h^2/Q^{(0)}$ . [Figure 10\(a\)](#) shows the energy growth envelope for plane Poiseuille flow for this case with  $t_{Orr}$  marked by the red line. In [figure 10\(b\)](#), we compare the growth rate wiggles for different pulsation frequencies to this transient growth time scale. We see that the growth bursts all happen on the same time scale that compares very well with the time scale of the Orr mechanism.

In a second step, we take a closer look at one particular case,  $Wo = 18$ ,  $\tilde{Q} = 0.16$  ([figure 9e](#)), where the wiggles are particularly pronounced. In [figure 11](#), the variation of the dominant subharmonic eigenvalue orbit during the damping phase is shown together with snapshots of the streamwise velocity component of the associated eigenvectors as well as the linear perturbation for the full the branch transition. This parameter combination highlights the typical features of the branch transition while the dominant permutation

Subharmonic eigenvalue orbits in pulsating Poiseuille flow

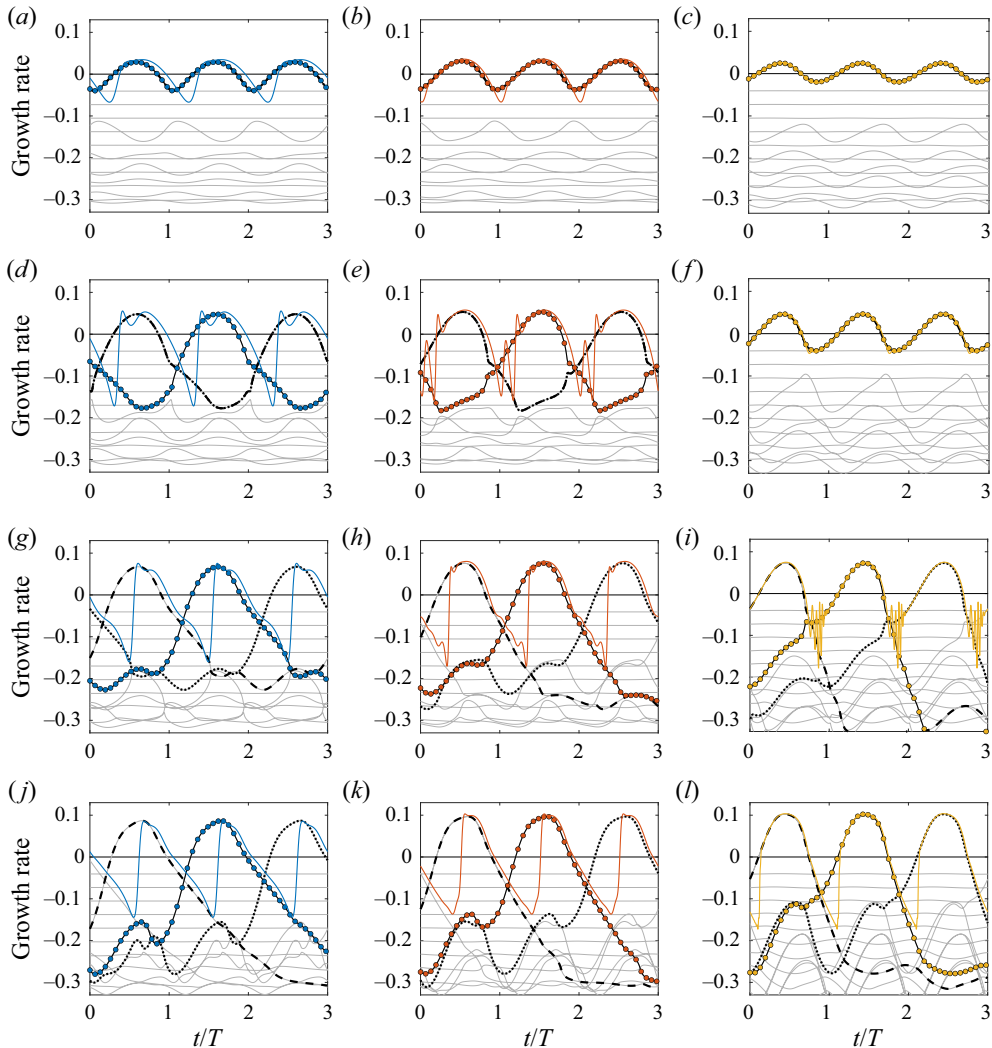


Figure 9. Evolution of the perturbation growth rate (thick coloured line) after the transients have passed compared with the real part of the instantaneous symmetric spectrum (grey lines) over three consecutive periods for different pulsation frequencies and amplitudes at  $Re = 7500$ . The dominant eigenvalue orbit is highlighted and, if it is subharmonic, the same orbit in adjacent periods are marked in black as dotted and dashed lines. In these cases, a movie comparing flow fields of the linear perturbation with the instantaneous eigenvectors of adjacent branches of the dominant orbit are available in the supplementary material (linked in the description). Here (a–c)  $\tilde{Q} = 0.08$ ; (d–f)  $\tilde{Q} = 0.18$ ; (g–i)  $\tilde{Q} = 0.28$  (j–l)  $\tilde{Q} = 0.50$ . Here (a,d,g,j)  $W_0 = 25$  (blue); (b,e,h,k)  $W_0 = 18$  (red); (c,f,i,l)  $W_0 = 10$  (yellow).

cycle only contains two eigenvalues which makes the presentation more clear. The essential features of the transition process are the same in all cases considered in this work.

Let us first analyse the variation of the instantaneous eigenstates along the two branches  $u_0$  and  $u_1$  of the dominant subharmonic orbit before comparing it with the linear perturbation.

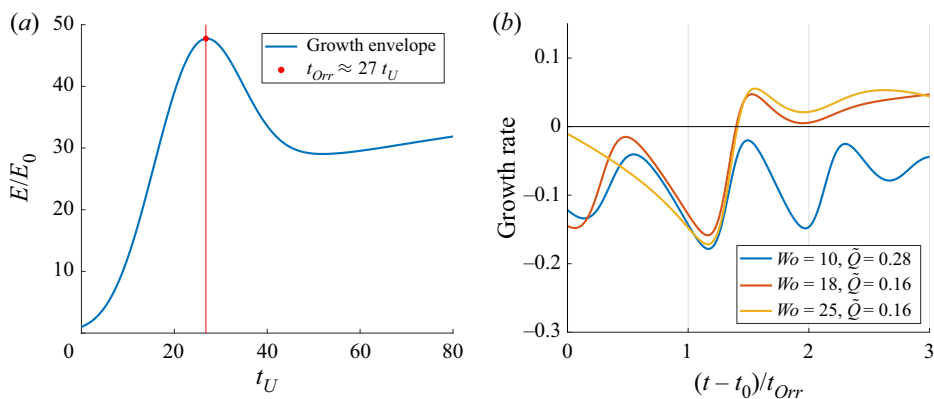


Figure 10. Definition of the non-normal growth time scale  $t_{Orr}$ . (a) Growth envelope for maximum transient growth for plane Poiseuille flow at at  $Re = 7500$  and  $\alpha = 1$ . The energy maximum at  $t_{Orr}$  is indicated with a red dot. (b) Superposition of the wiggles in the growth rates of for three configurations with time scaled by  $t_{Orr}$ . Since the wiggles occur at very different times in each case, the curves are shifted by  $t_0$  (different in each case) to facilitate direct comparison.

At the beginning of the considered section, which corresponds to the end of the amplification phase ( $t_1$ ), we observe that the two branches of the orbit are very different, both in terms of growth rate and in spatial structure. With the beginning of the damping phase ( $t/T = 0.80$ ), the eigenstates (eigenvalues and eigenvectors) quickly converge and are very similar at  $t_2$ . This point is very close to the EP at which the subharmonic orbit formed and of which the minimum of the angle  $\theta$  is the vestige. Their paths subsequently diverge again. During the damping phase, the growth rate of  $u_0$  drops as the vortices of the eigenvector are sheared by the base flow and move away from the wall ( $t_2$  and  $t_3$ ). The imaginary part of the eigenvalue reflects the increased base flow velocity at the location of the dominant vortex row by steadily increasing up until  $t_4/t_5$  where the heavily sheared vortices of the eigenvector  $u_0$  stop moving towards the centreline. Simultaneously, the growth rate of  $u_1$ , which was very damped at  $t = t_1$ , increases continuously, passing  $u_0$  at  $t_3$  and changing sign at  $t_7$  thus initiating the amplification phase. In contrast to  $u_0$ , for which the vortices move to the centreline while experiencing intense shear, the eigenvector of  $u_1$  is pushed towards the wall which is echoed by a decrease of the imaginary part (phase speed) of the corresponding eigenvalue. These two opposite effects lead to the large difference in phase speeds between  $u_0$  and  $u_1$  that we observe throughout the damping phase.

Consider now the evolution of the linear perturbation  $u_{lin}$  in the limit cycle over the same period and how it relates to the instantaneous eigenvectors described above.

Initially, the perturbation is aligned with the direction  $u_0$  exhibiting the structure of modulated Tollmien–Schlichting waves typical of the amplification phase of pulsating Poiseuille flow ( $t_1$ ). The subsequent variation of the eigenvectors heralding the damping phase is too rapid to be followed instantaneously by the linear perturbation and we observe that the growth rate only slowly decreases and changes sign at  $t_2$  with considerable delay compared with  $u_0$ . The vortices in the linear perturbation are soon also sheared with the mean flow which is accompanied by strong damping ( $t_3$ ). In the subsequent phase, all eigenvalues are damped and the linear perturbation has a non-zero projection on both  $u_0$  and  $u_1$  that are far from orthogonal during the branch transition process and can thus lead to non-normal growth. In fact, we see the footprint of both eigenvectors in the perturbation

Subharmonic eigenvalue orbits in pulsating Poiseuille flow

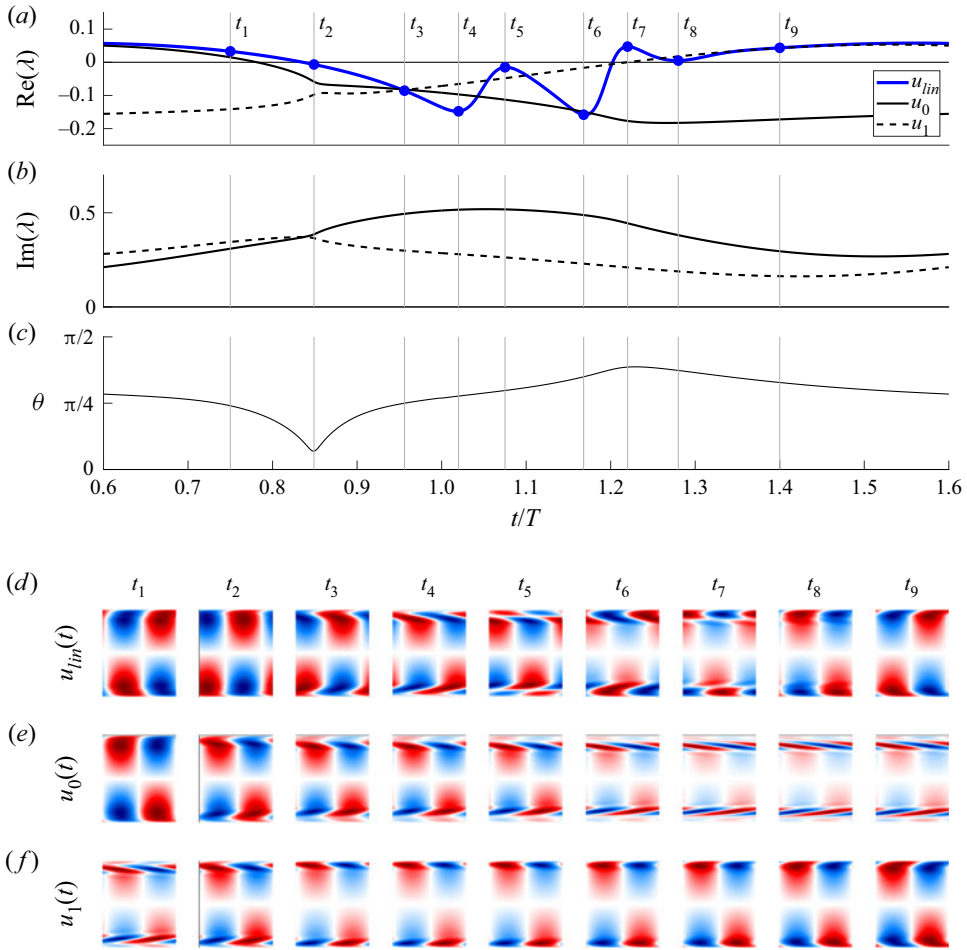


Figure 11. Variation of the streamwise velocity field and the growth rate of the linear perturbation centred on the branch transition compared with the dominant eigenstate orbit at  $Re = 7500$ ,  $Wo = 18$ ,  $\tilde{Q} = 0.16$  (same case as in figure 9e). (a–c) Variation of the real and imaginary parts ((a) and (b), respectively) of the instantaneous eigenvalues along the subharmonic orbit  $\varphi_1^s$  (black lines) compared with the growth rate of the linear perturbation (thick blue line). The two branches of  $\varphi_1^s$  are distinguished by the dashed and full linestyles and the angle  $\theta$  (in radians) between the corresponding eigenvectors is shown in panel (c). (d–f) Instantaneous streamwise velocity fields of the linear perturbation and eigenvectors of  $\varphi_1^s$ , each column corresponding to a time instant marked by a vertical line in (a–c). Panel (d) corresponds to the linear perturbation ( $u_{lin}$ ) whereas the panel (e, f) shows the instantaneous eigenvectors of the branches  $u_0$  (full black line) and  $u_1$  (dashed line) of  $\varphi_1^s$ . The y-direction is the wall-normal direction and the x-direction is the streamwise direction. A movie of the variation in time is available in the supplementary material (movie 2).

field which exhibits a row of vortices close to the wall ( $u_1$ ) as well as sheared vortices closer to the centreline ( $u_0$ ). The wiggles in the growth rate occur due to the rapid changes in the structure of  $u_{lin}$ . The difference in phase speed of the eigenvectors related to the difference in magnitude of the imaginary parts of  $u_0$  and  $u_1$  leads to a large relative velocity difference in the streamwise translation of the vortex rows in the linear perturbation. It is the interaction of these vortices that creates the strong variations in the growth rate we see in the perturbation in figure 11(a–c). During each growth burst, the vortex rows begin paired with alternating orientations. As the faster moving inner vortex row moves ahead of

the outer row, the vortices of the same orientation merge to form large structures leaning against the mean shear extracting energy from the base flow in a manner analogous to the Orr mechanism generating large growth ( $t_5$  and  $t_7$ ). Subsequently, the vortices experience a strong decay when they are sheared with the mean shear ( $t_4$  and  $t_5$ ). During the branch transition process, the focus of the perturbation steadily moves from the vortices close to the centreline to the vortex row close to the wall together with the increasing growth rate gap in the corresponding instantaneous eigenvalues. As soon as  $u_1$  starts to be amplified  $t_7$ , the wiggles quickly disappear as  $u_{lin}$  aligns with the newly amplified eigenvector ( $t_8$  and  $t_9$ ).

In order to allow the reader to fully appreciate the similarities and differences across the considered parameter range, we have created a movie that is available in the supplementary material comparing the evolution of the linear perturbation with the instantaneous eigenstates in terms of both the growth rate and the spatial structure for the case shown in [figure 11](#) where the leading eigenvalue has joined a permutation cycle and thus branch transition occurs.

Based on this analysis, the wiggles in the instantaneous growth rate observed during the branch transition process are indeed caused by repeated non-normal instantaneous transient growth bursts that are very similar to the Orr mechanism. All the cases considered in this work exhibiting a branch transition follow the same path.

### *5.3. Instantaneous non-normal growth and Floquet eigenfunctions in periodic flows*

Time-periodic flows such as pulsating Poiseuille flow are special cases of time-dependent flows for which the time-asymptotic behaviour of a linear perturbation can be represented by the Floquet eigenfunctions (Davis 1976). The variations of the growth rate during the pulsation cycle that we have identified as non-normal growth bursts are included and contribute to the Floquet multipliers that quantify the cycle-to-cycle growth of the eigenfunctions. This fact does not preclude an analysis of the growth bursts as instantaneous phenomena linked to the local eigenvalue spectra in time. The leading Floquet eigenfunction is, in fact, identical to the solution of the linear IVP after the initial transients have passed, as computed in this study using a time stepper approach; whether the instantaneous transient growth bursts are understood as manifestations of the global dynamics (Floquet) or an instantaneous effect of the local (in time) dynamics differs only in the interpretation.

The local interpretation of transient growth that we propose here is useful for two reasons. On the one hand the direct comparison with the local spectra elucidates the instantaneous growth mechanism allowing for the distinction of phases dominated by modal or non-modal growth within the pulsation cycle. This analysis is not directly possible within the Floquet framework since it involves a Fourier transform and is therefore delocalised in time. On the other hand, the interpretation of instantaneous growth in terms of local spectra can be extended to non-periodic time-dependent cases where Floquet theory cannot be applied, given a sufficient time scale separation between viscous/inertial time scales of the flow and the imposed time-dependence. In the case of arbitrary time-dependence of the flow without scale separation the local approach is questionable. A possible way forward in this scenario is the analysis of the left and right singular vectors of the fundamental solution matrix (see, e.g. Schmid 2007).

Due to the special care that needs to be taken when applying the nomenclature related to transient and non-normal growth, typically discussed in steady scenarios, in a time-dependent setting, we propose a disambiguation in the [Appendix B](#).



## Subharmonic eigenvalue orbits in pulsating Poiseuille flow

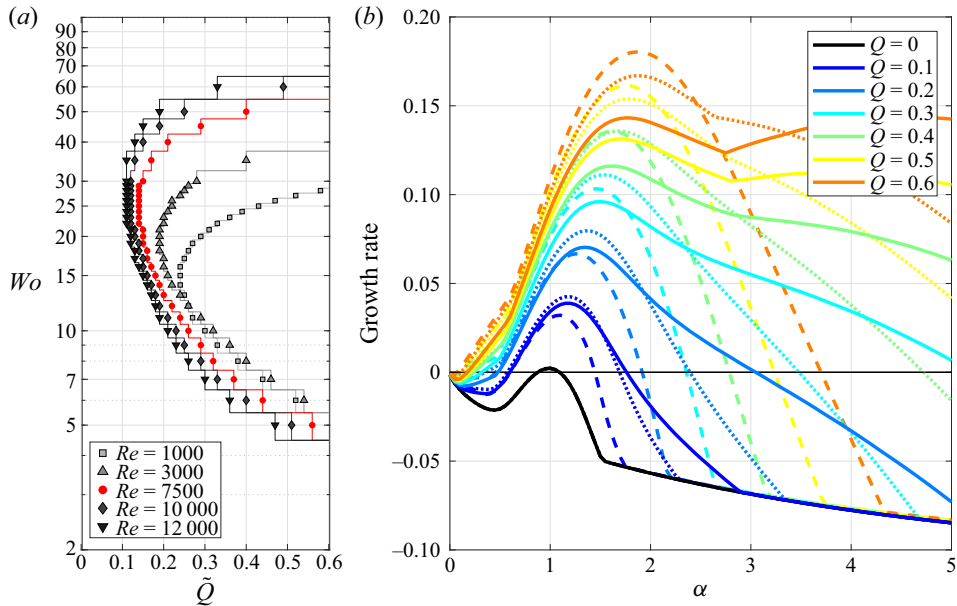


Figure 12. (a) Same as figure 4(b) but showing the appearance of the first subharmonic orbit involving the dominant symmetric eigenvalue for different Reynolds numbers. The red line is the same as the limit of the coloured area in figure 4(b). (b) Growth rate of the most amplified wavenumber for different pulsation amplitudes at  $Re = 7500$  and for  $Wo = 10, 18, 25$ , (dashed, dotted and full lines, respectively).

### 5.4. Variation of the spanwise wavenumber and the Reynolds number

In this study, we have restricted the detailed analysis to the two-dimensional configuration with a streamwise wavenumber  $\alpha = 1$  and a Reynolds number of 7500, which is slightly supercritical in the corresponding steady case. In order to assess the general validity of our approach and analysis also beyond the scope of the chosen parameter range, it is important to consider the effect of a variation of the Reynolds number and the streamwise wavenumber  $\alpha$ .

The Reynolds number governs the viscous time scale (i.e. the time scale on which viscosity is dominant) of the system and measures the ratio of inertial to viscous forces in the flow. In general, an increase (decrease) of the Reynolds number leads to a decrease (increase) of the base flow stability and sparsity of the spectrum (i.e. the distance between neighbouring eigenvalues) but the non-normality remains. We know that for intermediate values of the Womersley number, the pulsations lead to increasingly large excursions of the eigenvalues, both in term of growth rate and phase speed, and the formation of EPs as the pulsation amplitude grows. In terms of the spectrum and the emergence of subharmonic orbits, an increase of the Reynolds number leads to larger excursions of the eigenvalues over a pulsation cycle and, in general, earlier formation of subharmonic orbits, and *vice versa*. Since the non-normal growth potential decreases with the Reynolds number, the transient growth bursts during branch transitions follow suit. Figure 12(a) shows how the Reynolds number affects the appearance of subharmonic eigenvalue orbits (only the symmetric case is shown).

The streamwise wavenumber  $\alpha = 1$  for this study was chosen close to the most unstable spanwise invariant configuration for steady Poiseuille flow. When pulsations are added, we

observe not only a large variation of the instantaneous spectrum but also a shift in the most amplified streamwise wavenumber over the course of the pulsation cycle. Figure 12(b) shows, for each wavenumber, the maximum growth rate of the dominant eigenvalue of the local spectra at any time during the pulsation cycle. As expected, the maximum growth rates increase for all wavenumbers with the pulsation amplitude, irrespective of the pulsation frequency. At the same time the overall most amplified wavenumber shifts to slightly higher values.

In spite of these differences, the solutions to the IVP in the periodic regime do not change qualitatively. Since the time scale ratio  $\mathcal{T}$  is inversely proportional to the Reynolds number, a decrease of the Reynolds number leads to an increase of the time scale ratio (and *vice versa*) meaning that the viscous time scale becomes slower relative to the pulsation time scale and the linear solution lags behind the instantaneous spectra even for low values of the Womersley number.

### 5.5. Outlook on three-dimensional perturbations

Given the well known fact that three-dimensional perturbations often generate far greater transient growth than their two-dimensional counterparts and, moreover, that the recent study of Pier & Schmid (2021) has shown that the mechanism for optimal initial transient growth can be either two-dimensional or three-dimensional depending on the parameter configuration, it is a natural next step to ask whether the bursts during the transition process will exhibit a similar behaviour.

The mathematical properties that give rise to EPs and thereby lead to the formation of subharmonic eigenvalue orbits, i.e. the non-normality of the linear operator, do not depend on the spatial structure of the perturbations considered. If anything, the additional parameter makes the appearance of EPs more likely. Therefore, the results regarding the appearance and distribution of the eigenvalue permutation cycles in the considered parameter space vary only quantitatively as the spanwise wavenumber is varied and are not shown here.

In this work, only two-dimensional perturbations were considered in detail to keep the parameter space manageable. Since the qualitative behaviour of EPs and subharmonic eigenvalue orbits is the same as for the two-dimensional case and we have data regarding optimal energy growth (Pier & Schmid 2021) for the three-dimensional case, we can speculate about the effect of allowing three-dimensional perturbations on the solution of the linear IVP.

The existence of subharmonic eigenvalues orbits involving the leading eigenvalue also when  $\beta \neq 0$  implies the necessity of branch transitions in the periodic regime in these cases likely driven by non-normal growth bursts. Considering that, as Pier & Schmid (2021) note, ‘streamwise-invariant ( $\alpha = 0$ ) perturbations appear to be almost unaffected by the time-dependent component of the base flow and to display a dynamics predominantly dictated by the time-averaged base flow’, it is unlikely that a considerable streamwise-invariant component of the perturbation is part of the intrinsic linear dynamics of pulsating Poiseuille flow which fully determine the solution in the time-asymptotic periodic regime. Hence the authors expect the behaviour of the linear IVP allowing for three-dimensional perturbations to be qualitatively similar in the periodic regime to the results shown here, in particular regarding the nature of the non-normal growth bursts via a predominantly two-dimensional mechanism.

## 6. Summary and conclusion

In the following we discuss the main findings of this paper that follow two main lines. First, we consider the occurrence of EPs in the spectrum of the local OS problem for pulsating Poiseuille flow over a wide range of pulsation frequencies and amplitudes that lead to the formation of subharmonic eigenvalue orbits. The second part focuses on the effect of these eigenvalue permutation cycles on the evolution of linear perturbations on top of the base flow with particular emphasis on the wiggles in the growth rate during the damping phase.

Eigenvalue degeneracies and their impact on the linear stability have been discussed for a number of canonical flow cases (Gaster (1968), Gustavsson & Hultgren (1980), Koch (1986), Shanthini (1989), Reddy & Henningson (1993), among others). We consider a specific type of degeneracy, namely EPs, mentioned in passing by Grosch & Salwen (1968), that are in fact ubiquitous in the spectrum of pulsating Poiseuille flow.

In this work, the prevalence of subharmonic eigenvalue orbits in the spectrum of two-dimensional pulsating Poiseuille flow was studied at  $Re = 7500$  for a streamwise wavenumber of  $\alpha = 1$  for a wide range of pulsation frequencies and amplitudes. We will summarise the results of the spectral analysis for these cases here.

- (i) For very low pulsation amplitudes, all eigenvalues form isolated periodic orbits at the base flow frequency around the locus of the steady spectrum.
- (ii) The first subharmonic orbits form with the merging of neighbouring orbits in the junction region of the eigenvalue branches. The lowest pulsation amplitude that was found to sustain a subharmonic eigenvalue orbit is  $\hat{Q} = 0.07$  at a frequency of  $Wo = 18$ . As the pulsation amplitude is further increased, subharmonic orbits become ubiquitous and the eigenvalue permutation cycles soon encompass most of the eigenvalues with the exception of the least stable centre modes (P-branch) and highly damped eigenvalues of the S-branch.
- (iii) Subharmonic orbits are most abundant for intermediate pulsation frequencies where the base flow pulsations have a similar time scale as the intrinsic instability waves in Poiseuille flow and the eigenvalue excursions over the cycle are largest. In this parameter region there are generally only two subharmonic orbits (one for each symmetry) encompassing more and more eigenvalues from the A-branch and the junction region as the pulsation amplitude is increased.
- (iv) At higher/lower pulsation frequencies, the large permutation cycles disintegrate into a number of separate and smaller orbits. For very high and very low pulsation frequencies, the emergence of subharmonic orbits is increasingly delayed to higher pulsation amplitudes. In the limiting cases of QS flow ( $Wo \rightarrow 0$ ) as well as high-frequency base flow oscillations ( $Wo \rightarrow \infty$ ), the formation of subharmonic orbits is entirely suppressed.
- (v) We confirm the conjecture of earlier studies (Kern *et al.* 2021) that the maximum non-normal growth potential at higher pulsation frequencies is largely unchanged compared with steady Poiseuille flow. The variation at low pulsation frequencies can be fully explained by the variation of the effective Reynolds number and does not depend on the details of the base flow profile.

In the light of the existence of EPs that lead to subharmonic eigenvalue orbits in the spectrum of pulsating Poiseuille flow, it is interesting to analyse their impact on growth and decay of linear perturbations on the base flow. Although the eigenvalue degeneracies themselves do not seem to have any visible effect on the evolution of a linear perturbation, the formation of subharmonic eigenvalue orbits involving the dominant eigenvalue leads to necessary transitions from the decaying to the amplified branch of the orbit. In the

following we will summarise the results concerning the solution to the linear IVP and in particular the analysis of the branch transition process.

- (i) The evolution of the linear perturbation is smooth with respect to all parameters, even close to a spectral degeneracy.
- (ii) The perturbation continuously aligns with the instantaneously most unstable eigendirection. The alignment, although never complete, is more pronounced when the growth rates are large and the operator changes slowly (low pulsation frequency). When the operator changes rapidly or when there are several competing eigenstates with projections on the instantaneous perturbation, the alignment is worse or completely lost (high pulsation frequencies and damping phases when subharmonic orbits exist).
- (iii) When subharmonic orbits exist, the perturbation will necessarily transition from the decaying branch to the amplified branch of the dominant orbit at some point during the cycle since the perturbation has the same frequency as the base flow in the periodic regime.
- (iv) The branch transition is accompanied by growth rate wiggles for all considered parameter combinations as the pulsation amplitude is increased and have a similar characteristic time scale,  $t_{Orr}$ , which is the time scale of the transient growth generated via the Orr mechanism for two-dimensional optimal disturbances. The wiggles are identified as transient growth bursts generated by the interaction of non-orthogonal instantaneous eigendirections.
- (v) Although the details and amplitudes are highly dependent on the parameter combination, the non-normal growth bursts that constitute the branch transition process in all considered cases generate energy growth via the Orr mechanism.

In this work we have shown that subharmonic eigenvalue orbits, brought about by the existence of EPs, are ubiquitous in the periodic spectrum of the OS operator for two-dimensional pulsating Poiseuille flow for a large range of pulsation amplitudes and frequencies of practical interest. When such subharmonic permutation cycles occur, the difference in temporal periodicity of the eigenvalue orbits compared with the evolution of a linear perturbation, asymptotically periodic with the base flow frequency, leads to periodic branch transitions as the disturbance aligns with the instantaneously unstable eigendirection. These transitions towards the amplified branch are shown to occur via a series of non-normal growth bursts involving the interaction of non-orthogonal modes from different branches of the subharmonic cycle similar to the Orr mechanism in steady Poiseuille flow. These results show that, while they are not the main driving mechanism for non-modal growth, spectral degeneracies and in particular EPs can have significant impact on the spectral characteristics of the periodic OS operator that reflect on the evolution of linear disturbances.

**Supplementary movies.** Supplementary material and movies are available at <https://doi.org/10.1017/jfm.2022.515>.

**Acknowledgements.** The authors thank M. Beneitez for helpful discussions on the OTD modes and the subharmonic orbits as well as the help in implementing the OTD modes in MATLAB.

**Funding.** Financial support for this work was provided by the European Research Council under grant agreement 694452-TRANSEP-ERC-2015-AdG and by the Swedish Research Council (VR) grant no. 2016-03541.

**Declaration of interests.** The authors report no conflict of interest.

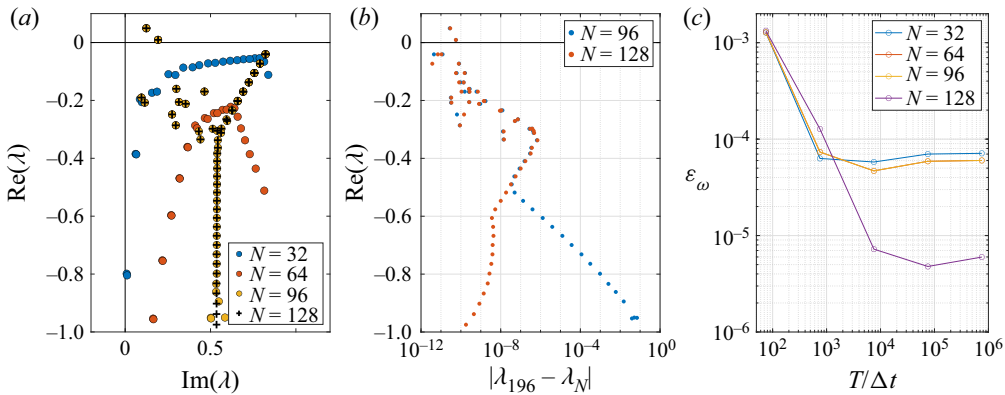


Figure 13. Resolution studies. (a,b) Eigenvalue problems: eigenvalue spectra of the OS operator and error for different spatial resolutions for  $Re = 7500$ ,  $\alpha = 1$ ,  $Wo = 25$ ,  $\bar{Q} = 0.2$  using the base flow profile at  $t/T = 0.5$ . (c) Linear IVPs: error in the real temporal growth rate (real part of the Floquet exponent) computed as the integral over one period of the instantaneous growth rates  $\gamma$  compared with the values from Kern *et al.* (2021) for  $Re = 7500$ ,  $\alpha = 1$ ,  $Wo = 25$ ,  $\bar{Q} = 0.2$  using different spatial ( $N$ ) and temporal ( $\Delta t$ ) resolutions.

Author ORCIDs.

-  J.S. Kern <https://orcid.org/0000-0002-2460-578X>;
-  A. Hanifi <https://orcid.org/0000-0002-5913-5431>;
-  D.S. Henningson <https://orcid.org/0000-0001-7864-3071>.

Appendix A. Numerical solution of the eigenvalue problems and linear IVPs and link to OTD modes

The eigenvalue problems are discretised in the wall-normal direction using the Chebyshev collocation technique. The differential operators are computed using the dmsuite software package (Weideman & Reddy 2000). Within the package, the Dirichlet boundary condition at the walls is implemented by omitting the boundary points from the equation system for which the solution is known, while the Neumann condition on the first derivative is implemented via Hermite interpolation.

The error in the computation of the eigenspectra as a function of the wall-normal resolution are shown in figure 13(a,b) for a particularly inflectional base flow profile. In order to capture the transient growth bursts that rely on damped eigenvalues, a spatial resolution of  $N = 128$  was chosen where the relevant part of the spectra is fully converged.

The wall-normal symmetry of the base flow can be leveraged to reduce the size of the eigenvalue problems to  $N_s = N/2$  by imposing the symmetry in the operator and solving for the symmetric (varicose) and antisymmetric (sinuous) modes separately.

The time integration of the linear IVP (3.18) was implemented using a four-step Runge–Kutta scheme. The full three-dimensional operator (of order  $2N$ ) is computed using the analytical expression for the base flow at each time step. When considering only two-dimensional perturbations ( $\beta = 0$ ), only the OS equation is solved, reducing the problem size to order  $N$ . The wall-normal symmetry was not implemented in the time integration.

Figure 13(c) shows the evolution of the error in the time integration for different choices of time step  $\Delta t$  and  $N$  for  $Wo = 25$ , the case with the shortest pulsation period  $T = 75.4$ . With the spatial resolution of  $N = 128$ , a time step of  $\Delta t = 10^{-3}$  was chosen

( $T/\Delta t = 7.5 \times 10^4$ ). It was carefully checked that the details of the growth rate wiggles do not depend on the spatial or temporal resolution.

The OTD modes are a recent framework to compute a time-dependent orthonormal basis that spans the instantaneously most unstable directions of the tangent space of nonlinear systems (Babae & Sapsis 2016). In order to generate the basis vectors and avoid their collapse on the most unstable direction, the orthonormality constraint is included directly into the linear evolution equations (3.18) yielding the OTD equations for each basis vector  $q_i$  (Blanchard & Sapsis 2019) given by

$$\frac{\partial q_i}{\partial t} = Lq_i - \langle Lq_i, q_i \rangle_E q_i - \sum_{j=1}^{i-1} (\langle Lq_i, q_j \rangle_E + \langle Lq_j, q_i \rangle_E) q_j, \quad i = 1, \dots, r, \quad (\text{A1})$$

where  $L$  is the linear operator,  $\langle \cdot, \cdot \rangle_E$  is the energy norm and  $r$  is the number of orthonormal basis vectors.

For the computations involving the OTD modes,  $r$  linear problems of the form (3.18) are solved simultaneously, coupled via additional nonlinear forcing terms  $f_i$  for each OTD basis vector  $q_i$ ,  $i = 1, \dots, r$ , which are computed explicitly at every step as

$$f_i = -\langle Lq_i, q_i \rangle_E q_i - \sum_{j=1}^{i-1} (\langle Lq_i, q_j \rangle_E + \langle Lq_j, q_i \rangle_E) q_j. \quad (\text{A2})$$

In practise, the resulting basis vectors need to be reorthonormalised at regular intervals to avoid the collapse of the OTD subspace (Kern *et al.* 2021).

## **Appendix B. Disambiguation of the term transient growth in the context of time-dependent flows**

Transient growth, i.e. the short-lived energy amplification of particular states due to the interaction of non-orthogonal eigendirection of non-normal operators, was originally described for steady flows and has since been tightly linked to the concept of optimal initial conditions for energy growth. For these cases, since almost all perturbations eventually align with the dominant eigendirection and are asymptotically governed by the corresponding modal growth rate, transient growth becomes effectively synonymous with initial transient growth since it can only occur at the beginning of the considered time window.

In the context of time-dependent flows this is not the case. Since the linear operator and hence its eigendirections are constantly evolving, the potential for non-modal growth is present at all times, depending on the projection of the perturbation onto the instantaneous eigendirections. This does not mean that the evolution of the perturbation therefore must be dominated by these non-normal effects at all times. In the same way that the initial transient growth can be entirely bypassed in a steady system if, e.g. the initial condition is chosen to be the dominant eigendirection, the perturbation in a time-dependent flow will only experience considerable non-modal growth in the right conditions.

Note here that the instantaneous non-normal growth a perturbation experiences due to a change in the operator at a specific time is, in general, lower than the maximum transient growth at the same instant (which is achieved for the first eigenvector of the symmetrised operator). Furthermore, the conditions that lead to non-normal growth in the time-asymptotic solution are a product of the linear dynamics alone and are independent of the initial conditions. In the case of periodic flows, only the linear dynamics on the



limit cycle are of interest for instantaneous non-normal growth once the initial transients have passed. Although the optimal disturbances for maximum energy growth may employ the same growth mechanism, the similarity is coincidental. They are generated via an optimisation over all possible initial conditions and do not take into account whether the corresponding state lies on the system's trajectory after the initial transients or not.

**Appendix C. Exact relation between the subharmonic eigenvalue orbits and the subharmonic orbits found with OTD modes**

The  $r$ -dimensional subspace spanned by the orthonormal basis vectors  $q_i$  is called an OTD subspace and spans the instantaneously most unstable directions in the phase space (Babae & Sapsis 2016). Comparing (A1) with the original IVP (3.18), we see that the basis vectors  $q_i$  are not solutions of (3.18) due to the forcing term with the exception of the first basis vector  $q_1$ , which is only constrained to change orthogonal to itself but otherwise follows the linearised dynamics.

In order to extract physically relevant information about the dominant directions in the subspace, we compute the reduced operator  $L_r \in \mathbb{C}^{r \times r}$  by orthogonal projection of the full operator  $L$  onto the OTD subspace. The eigenvalues of  $L_r$  together with the OTD modes, obtained by projecting the OTD basis vectors on the associated eigenvectors, correspond to the instantaneously most unstable directions of the tangent space (Babae & Sapsis 2016).

In a recent study applying the OTD framework to the case of pulsating Poiseuille flow, the authors reported that while for small subspace sizes the eigenvalues of  $L_r$  converged to periodic orbits with the same periodicity as the base flow, larger subspace sizes generated subharmonic eigenvalue orbits through the merging of several simple eigenvalue orbits (Kern *et al.* 2021).

In order to understand how the subharmonic eigenvalue orbits obtained from the OTD modes relate to the permutation cycles obtained by tracking the eigenvalues of  $L$  in time, we recall the definition of the reduced operator  $L_r$  in matrix form

$$L_r = Q_r^T L Q_r, \tag{C1}$$

where  $Q_r = [q_1, \dots, q_r]$ .

In case of a normal operator  $L$  for all times  $t$ , its eigenbasis is orthogonal and the OTD basis vectors (and also the OTD modes which coincide with the basis vectors in this case) converge to the  $r$  eigenvectors corresponding to the instantaneously least stable eigenvalues of  $L$  leading to a diagonal  $L_r$  (Babae & Sapsis 2016). For these operators, subharmonic eigenvalue orbits cannot occur since the existence of EPs requires non-orthogonal eigenvectors, and we therefore do not consider this case further.

If the operator  $L$  is non-normal, the OTD modes are in general different from the instantaneously least stable eigendirections of the underlying operator, with the exception of the limiting case  $r = n$ , where we have

$$L_n = Q_n^T L Q_n \tag{C2}$$

which is simply a change of basis and does not affect the eigenvalues. This means that the OTD modes will recover the orbits of the instantaneous eigenvalues of the underlying operator including the permutation cycles that appear with the presence of EPs. At an EP, two or more eigenvectors of  $L$  coalesce and its eigenbasis does not span the full  $\mathbb{C}^n$ . It has been shown that the OTD framework can deal with the instantaneous ambiguity due to eigenvalue crossings (Babae *et al.* 2017) which will be crucial in this application since crossing an EP is algorithmically similar to a generic eigenvalue crossing.

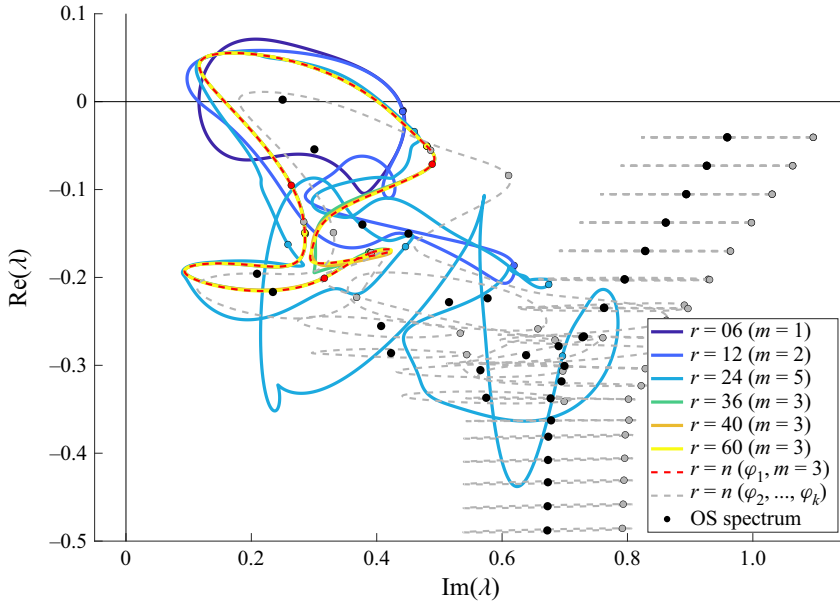


Figure 14. Variation of the eigenvalue orbits of the reduced operator  $L_r$  including the dominant eigenvalue using the OTD framework when increasing  $r$  from 6 to 60 (full lines) compared with the eigenvalue orbits  $\varphi_i$  computed from the full operator  $L$  (dashed lines) and the steady OS spectrum (black dots) for  $Re = 7500$ ,  $Wo = 25$ ,  $\tilde{Q} = 0.2$ . The eigenvalue orbit  $\varphi_1$  that includes the dominant eigenvalue is highlighted in red showing the convergence of the eigenvalue orbits of  $L_r$  as  $r$  is increased. The grey and coloured dots indicate the eigenvalue loci at the beginning of the corresponding cycle. The length  $m$  (in multiples of the base period  $T$ ) of each coloured orbit is indicated in parentheses in the legend.

For  $r < n$ , the situation is less clear. For small subspace sizes  $r$  that do not span a considerable portion of the full non-normal spectrum of  $L$ , the spectrum of  $L_r$  can be very different from the spectrum of  $L$ , especially if the highly non-orthogonal eigenvectors are associated with eigenvalues of very different growth rates. If the instantaneously fastest growing structure in the OTD subspace is due to the interaction of two such non-orthogonal eigenvectors of  $L$ , it will be identified by a single OTD mode (i.e. interpreted as a modal structure) as long as the second, more damped eigenvalue is not spanned by the subspace. In fact, the OTD subspace does not contain information about the eigenvectors of  $L$  or their relative orientation. Only when  $r$  is large enough to encompass the damped mode is this structure’s growth identified as a non-normal effect and therefore included in  $\sigma_{max}$  while the OTD modes subsequently follow the corresponding eigendirections of  $L$  (which, taken separately, exhibit a much lower modal growth). Since the OTD basis in the Blanchard & Sapsis formulation is hierarchical, i.e. adding more basis vectors does not affect the existing ones, the growth rate information they contain does not change as the OTD subspace is enlarged but is only reinterpreted as non-normal instead of modal growth.

The variation of the periodic orbits of the eigenvalues of the reduced operator  $L_r$  containing  $\lambda_1$  as the subspace size  $r$  is increased compared with the orbits obtained through eigenvalue tracking using local theory is presented in figure 14 and clearly shows convergence of the orbits computed using the OTD framework to the orbits of the full operator (dashed lines, in particular, the red dashed line). Note that, comparing with figure 3 where  $\varphi_1$  has a period of  $2T$  for  $\tilde{Q} = 0.15$ , the orbit has undergone one further coalescence in the range  $\tilde{Q} \in [0.15, 0.2]$  and now has period  $3T$ .

We observe that the convergence begins in the unstable part of the orbit of the corresponding eigenvalues since they are more likely to be spanned by the OTD subspace. Although, to the naked eye,  $\varphi_1$  is indistinguishable from the orbit of the corresponding eigenvalues of  $L_r$  at  $r = 60$ , we see that the convergence history is all but monotonic with the orbit first becoming much more complicated and spanning up to five periods ( $r = 24$ ) before homing in on the final orbit with period  $3T$  (red dashed curve). The seemingly chaotic orbit for  $r = 24$  is due to the fact that part of the orbit follows the most stable eigenvalue of the OTD subspace that shields the more unstable eigenvalues from the dynamics outside of the subspace but itself is very sensitive to eigenvalue crossings with modes just beyond the edge of the subspace. In order for the orbits to reliably represent a specific eigenvalue trajectory it needs to be spanned continuously during the entire cycle. This is ensured only if the most stable eigenvalue is not part of the considered orbit at any time because, in case of an eigenvalue crossing at the edge of the subspace, this eigenvalue will switch to a new eigenvalue and thus follow its orbit instead.

Although a good approximation of the eigenvalue orbits may be obtained in some cases using few OTD modes, a large subspace size  $r$  is required for their accurate computation for highly non-normal operators. In these cases, the OTD framework becomes exceedingly expensive since it requires the simultaneous solution of  $r$  IVPs of the form (3.18) in addition to the base flow trajectory and, if it is computationally feasible, the correlation based eigenvalue tracking is a far more efficient method for computing the subharmonic eigenvalue orbits. If, on the other hand, the full operator is not available explicitly (e.g. in matrix-free codes) or too large to analyse directly, the OTD modes are competitive in terms of computational cost for the approximation of subharmonic eigenvalue orbits, together with iterative eigenvalue methods such as the Arnoldi iteration to obtain the most unstable eigenvalues of the local problems involved in eigenvalue tracking methods.

#### REFERENCES

- BABAEI, H., FARAZMAND, M., HALLER, G. & SAPSIS, T.P. 2017 Reduced-order description of transient instabilities and computation of finite-time Lyapunov exponents. *Chaos* **27** (6), 063103.
- BABAEI, H. & SAPSIS, T.P. 2016 A minimization principle for the description of modes associated with finite-time instabilities. *Proc. R. Soc. Lond. A* **472**, 20150779.
- BENNEY, D.J. & ROSENBLAT, S. 1964 Stability of spatially varying and time-dependent flows. *Phys. Fluids* **7** (8), 1385–1386.
- BETCHOV, R. & CRIMINALE, W.O. 1966 Spatial instability of the inviscid jet and wake. *Phys. Fluids* **9** (2), 359–362.
- BLANCHARD, A. & SAPSIS, T.P. 2019 Analytical description of optimally time-dependent modes for reduced-order modeling of transient instabilities. *SIAM J. Appl. Dyn. Syst.* **18** (2), 1143–1162.
- BUTLER, K.M. & FARRELL, B.F. 1992 Three-dimensional optimal perturbations in viscous shear flow. *Phys. Fluids* **4** (8), 1637–1650.
- CHANG, M.-H., CHEN, F. & STRAUGHAN, B. 2006 Instability of Poiseuille flow in a fluid overlying a porous layer. *J. Fluid Mech.* **564**, 287–303.
- DAVIS, S.H. 1976 The stability of time-periodic flows. *Annu. Rev. Fluid Mech.* **8** (1), 57–74.
- DEMBOWSKI, C., GRÄF, H.-D., HARNEY, H.L., HEINE, A., HEISS, W.D., REHFELD, H. & RICHTER, A. 2001 Experimental observation of the topological structure of exceptional points. *Phys. Rev. Lett.* **86** (5), 787–790.
- D'ERRICO, J. 2021 Eigenshuffle, <https://www.mathworks.com/matlabcentral/fileexchange/22885-eigenshuffle>.
- DOPPLER, J., MAILYBAEV, A.A., BÖHM, J., KUHL, U., GIRSCHIK, A., LIBISCH, F., MILBURN, T.J., RABL, P., MOISEYEV, N. & ROTTER, S. 2016 Dynamically encircling an exceptional point for asymmetric mode switching. *Nature* **537** (7618), 76–79.
- FARRELL, B.F. 1988 Optimal excitation of perturbations in viscous shear flow. *Phys. Fluids* **31** (8), 2093–2102.
- GASTER, M. 1968 Growth of disturbances in both space and time. *Phys. Fluids* **11** (4), 723–727.
- GASTER, M. & JORDINSON, R. 1975 On the eigenvalues of the Orr–Sommerfeld equation. *J. Fluid Mech.* **72** (1), 121–133.

- GHANI, A. & POLIFKE, W. 2021 An exceptional point switches stability of a thermoacoustic experiment. *J. Fluid Mech.* **920**, R3.
- GROSCH, C.E. & SALWEN, H. 1968 The stability of steady and time-dependent plane Poiseuille flow. *J. Fluid Mech.* **34** (1), 177–205.
- GUSTAVSSON, L.H. 1986 Excitation of direct resonances in plane Poiseuille flow. *Stud. Appl. Maths* **75** (3), 227–248.
- GUSTAVSSON, L.H. & HULTGREN, L.S. 1980 A resonance mechanism in plane Couette flow. *J. Fluid Mech.* **98** (1), 149–159.
- HEISS, W.D. 2012 The physics of exceptional points. *J. Phys. A: Math. Theor.* **45** (44), 444016.
- JONES, C.A. 1988 Multiple eigenvalues and mode classification in plane Poiseuille flow. *Q. J. Mech. Appl. Maths* **41** (3), 363–382.
- KATO, T. 1976 *Perturbation Theory for Linear Operators*. 2nd edn. Die Grundlehren der mathematischen Wissenschaften, vol. 132. Springer.
- KERN, J.S., BENEITEZ, M., HANIFI, A. & HENNINGSON, D.S. 2021 Transient linear stability of pulsating Poiseuille flow using optimally time-dependent modes. *J. Fluid Mech.* **927**, A6.
- KOCH, W. 1986 Direct resonances in Orr–Sommerfeld problems. *Acta Mech.* **59** (1–2), 11–29.
- LEE, S.-B., YANG, J., MOON, S., LEE, S.-Y., SHIM, J.-B., KIM, S.W., LEE, J.-H. & AN, K. 2009 Observation of an exceptional point in a chaotic optical microcavity. *Phys. Rev. Lett.* **103**, 134101.
- LUITZ, D.J. & PIAZZA, F. 2019 Exceptional points and the topology of quantum many-body spectra. *Phys. Rev. Res.* **1**, 033051.
- MACK, L.M. 1976 A numerical study of the temporal eigenvalue spectrum of the Blasius boundary layer. *J. Fluid Mech.* **73** (3), 497–520.
- MENSAH, G.A., MAGRI, L., SILVA, C.F., BUSCHMANN, P.E. & MOECK, J.P. 2018 Exceptional points in the thermoacoustic spectrum. *J. Sound Vib.* **433**, 124–128.
- MILLER, J.L. 2017 Exceptional points make for exceptional sensors. *Phys. Today* **70** (10), 23–26.
- OR, A.C. 1991 On the behaviour of a pair of complex eigenmodes near a crossing. *Q. J. Mech. Appl. Maths* **44** (4), 559–569.
- ORR, W.M. 1907 The stability or instability of the steady motions of a perfect liquid and of a viscous liquid. Part II: a viscous liquid. *Proc. R. Irish Acad. A* **27**, 69–138.
- ORSZAG, S.A. 1971 Accurate solution of the Orr–Sommerfeld stability equation. *J. Fluid Mech.* **50** (4), 689–703.
- ÖZDEMİR, Ş.K., ROTTER, S., NORI, F. & YANG, L. 2019 Parity–time symmetry and exceptional points in photonics. *Nat. Mater.* **18** (8), 783–798.
- PIER, B. & SCHMID, P.J. 2017 Linear and nonlinear dynamics of pulsatile channel flow. *J. Fluid Mech.* **815**, 435–480.
- PIER, B. & SCHMID, P.J. 2021 Optimal energy growth in pulsatile channel and pipe flows. *J. Fluid Mech.* **926**, A11.
- REDDY, S.C. & HENNINGSON, D.S. 1993 Energy growth in viscous channel flows. *J. Fluid Mech.* **252**, 209–238.
- REDDY, S.C., SCHMID, P.J. & HENNINGSON, D.S. 1993 Pseudospectra of the Orr–Sommerfeld operator. *SIAM J. Appl. Maths* **53** (1), 15–47.
- SCHMID, P.J. 2007 Nonmodal stability theory. *Annu. Rev. Fluid Mech.* **39** (1), 129–162.
- SHANTHINI, R. 1989 Degeneracies of the temporal Orr–Sommerfeld eigenmodes in plane Poiseuille flow. *J. Fluid Mech.* **201** (1), 13–34.
- SOMMERFELD, A. 1908 Ein Beitrag zur hydrodynamischen Erklärung der turbulenten Flüssigkeitsbewegungen. In *Proceedings of the 4th International Congress of Mathematicians*, vol. III, pp. 116–124.
- SQUIRE, H.B. 1933 On the stability for three-dimensional disturbances of viscous fluid flow between parallel walls. *Proc. R. Soc. Lond. A* **142** (847), 621–628.
- TREFETHEN, L.N. 1997 *Numerical Linear Algebra*. Society for Industrial and Applied Mathematics.
- TREFETHEN, L. & EMBREE, M. 2005 *Spectra and Pseudospectra: The Behavior of Nonnormal Matrices and Operators*. Princeton University Press.
- TREFETHEN, L.N., TREFETHEN, A.E., REDDY, S.C. & DRISCOLL, T.A. 1993 Hydrodynamic stability without eigenvalues. *Science* **261** (5121), 578–584.
- VON KERCZEK, C.H. 1982 The instability of oscillatory plane Poiseuille flow. *J. Fluid Mech.* **116**, 91–114.
- WEIDEMAN, J. & REDDY, S. 2000 A matlab differentiation matrix suite. *ACM Trans. Math. Softw.* **26** (4), 465–519.
- ZHONG, Q. 2019 Physics and applications of exceptional points. PhD thesis, Michigan Technological University, <https://doi.org/10.37099/mtu.dc.etrdr/953>.